

POLITECNICO DI TORINO

---

M.Sc. in Electronic Engineering

Master's thesis

# Steerable metasurface antennas



**Advisor:**

Prof. Giuseppe Vecchi

**Co-advisors:**

Dott. Marco Righero

Dott. Francesco Vernì

**Laureando**

Lucia Teodorani

---

ACADEMIC YEAR 2019-2020

## Summary

Steerable antennas are capable of directing the radiating beam in directions externally specified. This feature is of extreme interest for satellite communications on-the-move (Satcom on the move), which is currently attracting a lot of attention. An important side requirement in this case is the extreme flatness of the desired antennas (especially for mass mounting on cars). It originated in radar applications, where the ability to steer the beam rapidly is useful for tracking moving objects. In currently available solutions, the beam steering is obtained either mechanically or electronically, in the form of phased array antennas. However, both these solutions have drawbacks: mechanical steering requires external components that can be subject to failure, and cannot be flat. Phased arrays are either very expensive (and used in defense scenarios, e.g.) or intrinsically beset with high losses in the array distribution network (beam-forming network).

Electronically reconfigurable metasurface antennas are promising to solve these open issues.

A metasurface is a two-dimensional arrangement of sub-wavelength unit cells. A simple example of this kind of surface is a texture of small (with respect to wavelength) metallic square patches of variable size, printed on a grounded dielectric substrate. Due to the sub-wavelength regime, the wave response to these structure is conveniently described in terms of a surface impedance - i.e. a relationship between the local (tangent) electric and magnetic fields. The spatial distribution of this surface impedance determines the radiation properties of the metasurface; hence, proper design of this impedance surface can allow obtaining the desired radiation pattern of the antenna.

In a second phase, the desired values of the surface impedance are realized by proper design of the sub-wavelength patterning. In the example of a texture of square patches, this feature is the *local* size of the patches.

A fundamental result is that a constant impedance surface (e.g. a pattern of identical square cells) produces a guided wave, i.e. a wave confined in the vicinity of the surface, that does not radiate any field outside. Instead, if the impedance surface is not spatially constant, i.e. modulated, the guided wave gets transformed into a wavefield that radiates away; this is called a *leaky* wave in the relevant literature. Hence, a leaky wave radiation arises from the perturbation (modulation) of a (surface) guided wave.

A very important fact is that the direction of beam radiated by the leaky wave depends on the phase velocity of the underlying guided wave. Hence, if one manages to control the velocity of this guided wave (i.e. its wavenumber), one eventually achieves the sought-for beam steering. Of course this should be done without harming the radiation mechanism of the leaky wave. Controlling this velocity of

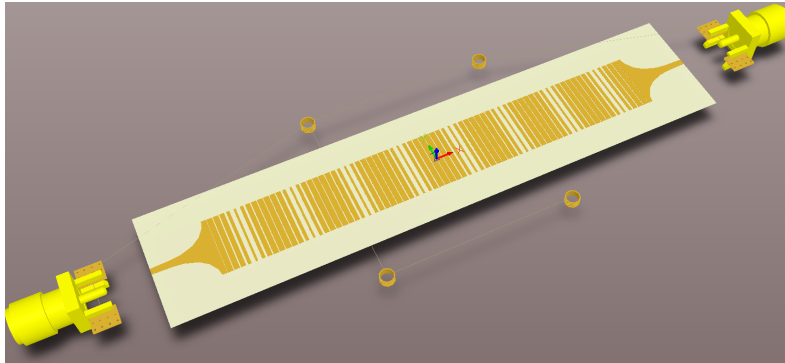


**Figure 1:** Simulated antenna: view of the upper layer, i.e. the sinusoidally-modulated reactance surface (SMRS). This is the one that generates radiation

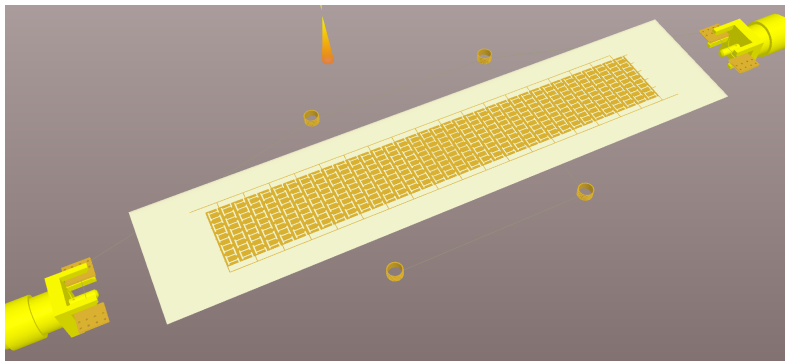
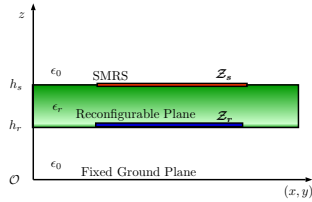


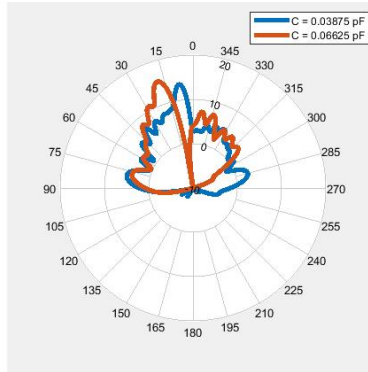
**Figure 2:** Simulated antenna: view of the middle layer, the electronically reconfigurable back-plane; the layout and circuit elements (varactors) result in a surface impedance whose value is voltage-controlled. This layer controls the phase velocity of the guided wave.

the guided wave in an electronic manner is the main contribution of this Thesis work.

To achieve our aim, we start from a leaky wave antenna with fixed beam (not scanning). It has an upper layer that produces a sinusoidally modulated impedance (reactance) surface (SMRS), via the variable-width metal strips shown in Fig.1. In the fixed-beam antenna, this patterning is on the top face of a dielectric sheet, and the back of this sheet is simply a metal plane ("ground"). To achieve steering, the metal backplane is substituted by a stacking of a ground plane and, above it, an electronically reconfigurable back plane (Fig.2). This produces a spatially constant surface impedance, that has a variable, voltage-controlled value. This control is achieved by the periodic repetition of a unit cell with varactor diodes across an ad-hoc portions of the unit cell. By changing the DC polarization voltage of



(a) 2D cut of the geometrical scenario



(b) Radiation pattern for two different antenna configurations; the main beam steers from  $8^\circ$  to  $19^\circ$

the varactors, one achieves variable capacitances; these in turn change the surface impedance of the back plane, and this produces a different phase velocity of the guided wave. This, as explained above, finally results in a variable direction of the radiated beam, that is then voltage-controlled.

Analyzing the structure, three different layers compose the steerable antenna (Fig.3a): on the bottom, there is a bare ground plane, separated by an air gap from the reconfigurable metasurface, Fig.2, which is surmounted by a dielectric layer and topped by a SMRS, Fig.1. The working principle is the following: changing the sheet impedance of the reconfigurable plane allows for the modification of the wavevector of the surface waves sustained by the structure and, consequently, of the surface impedance seen by such modes. The modulation of the overall surface impedance gives rise to a leaky wave radiating away from the surface at a certain angle, which depends on the average impedance and, ultimately, on the varactor diodes' capacitance.

State of the art systematic procedures allow deriving the admittance of a patterned metallic sheet, whether this is printed on a grounded dielectric substrate or not, starting from the scattering parameters. These techniques are tested and used to determine the sheet admittance of the upper layer of the proposed antenna. Then, the solution of the associated transverse resonance equation (TRE) gives the admittance of the reconfigurable plane. The smart design of the admittance, as mentioned earlier, plays a crucial role in achieving the maximum possible steerability of the main beam. Eventually, a proper unit cell layout, replicated in a periodic lattice, will implement such constant admittance values, given the range of capacitance of a commercial varactor diode at the frequencies of interest.

The complete antenna is simulated and designed using the full-wave electromagnetic solver CST. Despite some discrepancies between the expected results (based

on an approximate simplified model) and the simulations, the ultimate design has a clear steerability of the radiating beam, as can be seen from Fig.3b, which shows the radiation patterns for two different values of the varactor capacitance  $C$ .

# Contents

<b>List of Tables</b>	II
<b>List of Figures</b>	III
<b>1 Introduction</b>	1
1.1 Metasurface antennas . . . . .	1
1.2 Thesis Outline . . . . .	2
<b>2 Sheet admittance extraction methods</b>	3
2.1 Sheet extraction method for a printed-circuit tensor impedance surface	3
2.2 Sheet admittance from the scattering matrix . . . . .	7
<b>3 Dispersion relation</b>	9
3.1 Transverse resonance technique . . . . .	9
3.1.1 Example: mapping surface impedance to gap size . . . . .	9
3.1.2 Application to our multi-layered antenna . . . . .	11
3.2 Boundary conditions on tangential fields . . . . .	12
<b>4 Design of a Sinusoidally-Modulated Reactance Surface</b>	15
4.1 Theory . . . . .	15
4.2 Example: SMRS on a grounded substrate pointing at $30^\circ$ . . . . .	17
4.3 Application to our multi-layered antenna . . . . .	22
<b>5 Steerable leaky-wave antenna</b>	26
5.1 Implementation of the reconfigurable plane . . . . .	26
5.2 Simulation of the complete antenna . . . . .	28
5.3 Simulation of the complete antenna with bus . . . . .	33
<b>6 Conclusions</b>	38
<b>Bibliography</b>	40

# List of Tables

2.1	Sheet impedance values corresponding to the simulated geometry; all values are in $\Omega$ . . . . .	6
2.2	Sheet admittance values corresponding to the simulated geometry .	7
5.1	Expected and simulated radiation angle, directivity and side lobe level for different values of the varactor capacitance . . . . .	30
5.2	Expected and simulated radiation angle, directivity and side lobe level for different values of the varactor capacitance (antenna with buses) . . . . .	33

# List of Figures

1	Simulated antenna: view of the upper layer, i.e. the sinusoidally-modulated reactance surface (SMRS). This is the one that generates radiation . . . . .	ii
2	Simulated antenna: view of the middle layer, the electronically reconfigurable back-plane; the layout and circuit elements (varactors) result in a surface impedance whose value is voltage-controlled. This layer controls the phase velocity of the guided wave. . . . .	ii
2.1	Unit cell described in [1] replicated with CST . . . . .	4
2.2	Mesh of the unit cell described in [1] produced for the in-house solver; all dimensions are in m . . . . .	5
2.3	Unit cell in CST (a) and corresponding mesh for the in-house solver (b) . . . . .	8
3.1	Equivalent transmission-line model of a SMRS printed on a grounded dielectric substrate, as the one described in [2] . . . . .	10
3.2	Gap spacing vs surface reactance for the antenna designed in [2] obtained with CST and in-house solver . . . . .	11
3.3	Transmission-line model of our multi-layered antenna . . . . .	12
3.4	Vertical structure of our multi-layered antenna . . . . .	13
4.1	Brillouin diagram for $X_s = 1.2$ and $M = 0.2$ ; the blue curves correspond to the harmonics, the radiation cone is drawn in green, while the working point $k_0a$ is indicated by a red line . . . . .	16
4.2	Simulated antenna with detail of the SMRS . . . . .	18
4.3	Radiation pattern (cut for $\phi = 0^\circ$ ) of the antenna designed in [2] . .	18
4.4	Sheet admittance of a texture of square patches as a function of the gap between them . . . . .	19
4.5	Brillouin diagram of a SMRS with $X'_s = 0.3177$ and $M = 0.22$ . . .	20
4.6	Radiation pattern for a printed leaky-wave antenna with $X'_s = 0.3177$ , $M = 0.22$ and $a = 18$ mm . . . . .	20

4.7	Mapping between gap spacing and surface impedance for a SMRS made by square patches with dielectric RO4003C and thickness equal to 1.016 mm . . . . .	21
4.8	Radiation pattern (cut for $\phi = 0^\circ$ ) of the antenna with square patches; the main beam points at $32^\circ$ . . . . .	21
4.9	Detail of the SMRS with square patches . . . . .	22
4.10	Sheet admittance vs gap spacing of the SMRS . . . . .	23
4.11	Solutions of the transverse resonance equation for gap of the SMRS equal to 0.1 mm and two different values of $Y_{\text{VAR}}$ . . . . .	24
4.12	Solutions of the transverse resonance equation for gap of the SMRS equal to 0.1 mm and three different values of $Y_{\text{VAR}}$ . . . . .	25
5.1	Unit cell of the reconfigurable layer: (a) front view and (b) dimensions (mm) . . . . .	27
5.2	Sheet admittance of the reconfigurable metasurface with varying varactor capacitance . . . . .	27
5.3	Expected steering of the main beam with varying varactor capacitance	28
5.4	Front view of the antenna: SMRS and dielectric layer are clearly visible	29
5.5	Detail of the blending between middle layer and ground plane right below the feeder . . . . .	29
5.6	Simulated farfield (cut for $\phi = 0^\circ$ ) for different values of the varactor capacitance; the main beam steers from $2^\circ$ (a) to $25^\circ$ (d) . . . . .	31
5.7	Expected vs simulated steering of the main beam with varying varactor capacitance . . . . .	32
5.8	Front view of the reconfigurable layer (with ground plane in the background) with the addition of buses . . . . .	33
5.9	Example of the discontinuity in the mapping between gap width and surface impedance when the varactor capacitance (and therefore the sheet admittance $Y_{\text{VAR}}$ ) exceeds a limit value . . . . .	34
5.10	Radiation pattern for $C = 0.1$ pF ( $\theta = 28^\circ$ ) . . . . .	34
5.11	Simulated farfield for different values of the varactor capacitance (antenna with buses); the main beam steers from $1^\circ$ (a) to $21^\circ$ (d) .	36
5.12	Expected vs simulated steering of the main beam with varying varactor capacitance for the antenna with buses . . . . .	37
5.13	Upper layer of the steerable metasurface antenna . . . . .	37
5.14	Reconfigurable plane of the steerable metasurface antenna . . . . .	37

# Chapter 1

## Introduction

### 1.1 Metasurface antennas

Metasurfaces are periodic textures patterned at a sub-wavelength scale which are able to manipulate surface waves or to scatter incident waves in a peculiar manner [3]. Examples of metasurfaces are a texture of square patches printed on a grounded dielectric slab [4] or an array of metal strips separated by a gap [2]. The properties of this kind of surfaces can be summarized by a single parameter, namely the surface impedance [5]. In particular, the radiation mechanism of metasurface antennas is based on the modulation of such surface impedance, which is obtained by varying the geometrical parameter of the unit cell forming the metasurface, like the patch size [4] or the gap width [2]. The modulation of the surface impedance transforms a surface wave into a leaky wave, i.e. a wave that radiates energy while traveling along the antenna and, therefore, has a complex propagation wavenumber [6]. A leaky wave radiates away from the surface at an angle which depends on the phase constant, so it is possible to steer the beam by varying the working frequency.

What we aim to achieve in this work is the design of a steerable metasurface antenna that allows for beam scanning at a fixed frequency.

To do so, we plan to build a metasurface whose reactance is modulated sinusoidally (SMRS - Sinusoidally Modulated Reactance Surface) and place it above an electronically reconfigurable ground plane, i.e. a periodic arrangement of sub-wavelength cells whose reconfigurability is achieved through the insertion of varactor diodes in the unit cell. The goal is to reconfigure the impedance of the ground plane by varying the varactor diodes' capacitance, so that for different values of the DC driving voltage the antenna radiates at different controllable angles.

Ergo, the steerable metasurface antenna will be composed by three layers: on the bottom there is a bare ground plane, separated by an air gap from the reconfigurable metasurface, which is surmounted by a dielectric layer and topped by a SMRS. The working principle is the following: changing the sheet impedance of

the reconfigurable plane allows for the modification of the wavevector of the surface waves sustained by the structure and, consequently, of the surface impedance seen by such modes. The modulation of the overall surface impedance gives rise to a leaky wave radiating away from the surface at a certain angle, which depends on the average impedance and, ultimately, on the varactor diodes' capacitance.

## 1.2 Thesis Outline

This thesis is organized as follows: in **Chapter 2** state-of-the-art systematic procedures are described which allow to derive the sheet admittance of a patterned metallic metasurface, whether this is printed on a grounded dielectric substrate [1] or not [7], starting from the scattering parameters. The knowledge of the sheet admittance of every layer of our antenna is critical in order to obtain the overall surface impedance of the structure; such problem can be dealt with in different manners, all of which are reported in **Chapter 3**. In **Chapter 4** two SMRSs [2, 8] with different unit cells are studied as candidates for the realization of the upper layer of the antenna. As for the reconfigurable ground plane, its implementation is described in **Chapter 5**, together with the stack-up of the total antenna, which is then simulated and the results compared to the expected behavior. Finally, in **Chapter 6**, conclusions are drawn and future developments are teased.

# Chapter 2

## Sheet admittance extraction methods

In this chapter, systematic procedures are described which allow to derive the sheet admittance of a patterned metallic metasurface. In section 2.1 a technique to extract the sheet admittance of a printed-circuit tensor impedance surface is outlined, based on what is done in [1]. In section 2.2 another way to obtain these quantities is described which is applicable to a patterned metallic sheet that is not backed by a ground plane [7].

### 2.1 Sheet extraction method for a printed-circuit tensor impedance surface

The procedure to extract the sheet admittance of a printed-circuit tensor impedance surface (PCTIS) is described in detail in [1]. Here we summarize the main steps. One of the structures analyzed in [1] is then simulated with the full-wave electromagnetic solver CST [9] and an in-house solver in order to validate the repeatability of the aforementioned method.

Let's consider a unit cell - composed by ground plane, dielectric layer and patterned metallic cladding - placed in the  $xy$  plane, while the vertical stacking happens along  $z$ . The metallic sheet is therefore located at the interface between two regions, namely region 1 and 2, made of different materials, typically dielectric below (region 1) and air above (region 2). Two normal-incidence illuminations must be performed from above: one with the electric field polarized along  $x$  (illumination TM or A) and the other with the electric field directed along  $y$  (illumination TE or B). Then, from the total (incident plus scattered) electric and magnetic fields evaluated in region 2 at the  $z$  coordinate corresponding to the metallic sheet, the tensor

input admittance for normal incidence is derived using the following formulas:

$$Y_{xx}^{\text{in}} = \frac{E_y^{\text{A}} H_y^{\text{B}} - E_y^{\text{B}} H_y^{\text{A}}}{E_x^{\text{A}} E_y^{\text{B}} - E_x^{\text{B}} E_y^{\text{A}}} \quad (2.1)$$

$$Y_{xy}^{\text{in}} = \frac{E_x^{\text{B}} H_y^{\text{A}} - E_x^{\text{A}} H_y^{\text{B}}}{E_x^{\text{A}} E_y^{\text{B}} - E_x^{\text{B}} E_y^{\text{A}}} \quad (2.2)$$

$$Y_{yx}^{\text{in}} = \frac{E_y^{\text{B}} H_x^{\text{A}} - E_y^{\text{A}} H_x^{\text{B}}}{E_x^{\text{A}} E_y^{\text{B}} - E_x^{\text{B}} E_y^{\text{A}}} \quad (2.3)$$

$$Y_{yy}^{\text{in}} = \frac{E_x^{\text{A}} H_x^{\text{B}} - E_x^{\text{B}} H_x^{\text{A}}}{E_x^{\text{A}} E_y^{\text{B}} - E_x^{\text{B}} E_y^{\text{A}}} \quad (2.4)$$

At this point, the tensor sheet admittance is easily found:

$$\mathbf{Y}_{\text{sheet}} = \begin{bmatrix} Y_{xx}^{\text{in}} & Y_{xy}^{\text{in}} \\ Y_{yx}^{\text{in}} & Y_{yy}^{\text{in}} \end{bmatrix} - \begin{bmatrix} \frac{1}{j\eta_1 \tan(k_1 d)} & 0 \\ 0 & \frac{1}{j\eta_1 \tan(k_1 d)} \end{bmatrix} \quad (2.5)$$

where  $\eta_1$ ,  $k_1$  and  $d$  are the wave impedance, the wavenumber and the thickness of region 1 respectively.

The procedure just described is applied to the unit cell represented in figure 3 of [1] using CST (fig. 2.1). This implies setting *unit-cell* boundary conditions at  $x_{\min}$ ,

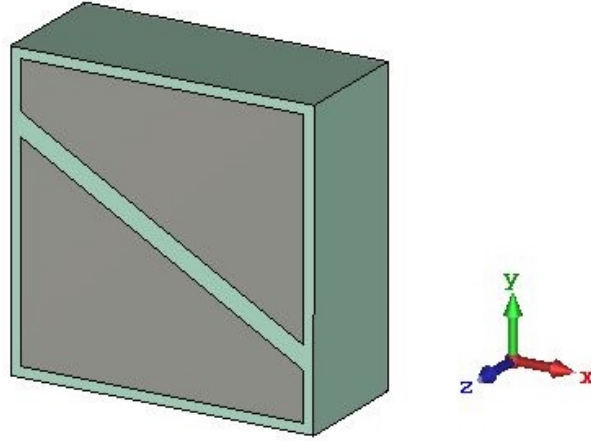


**Figure 2.1:** Unit cell described in [1] replicated with CST

$x_{\max}$ ,  $y_{\min}$  and  $y_{\max}$ , the condition  $E_t = 0$  at  $z_{\min}$  and open boundary at  $z_{\max}$ ; the last one automatically creates a Floquet port, that allows to excite the two different incident plane waves. The patterned metallic cladding is located at  $z = 0$ . The

fundamental point is to evaluate the average total electric and magnetic fields at this interface: the best way to do so is to measure the fields at a certain height from the surface (typically half a wavelength) and then de-embed the phases, in order to allow sufficient space for the highly oscillatory fields near the surface to subside [1]. However it is worth mentioning that CST calculates the required input admittance matrix automatically once we've set the reference plane for the de-embedding of the phase of the scattering parameters at  $z = 0$ . The tensor sheet admittance can then be computed using (2.5).

The same structure is analyzed with an in-house solver. The geometry of the patterned metallic cladding is drawn in Matlab, which allows also to elaborate its mesh (fig. 2.2). Such mesh, together with some files that contain the description of the structure scenario, is given as input to the solver. In general, the structure is composed by some layers of finite thickness, enclosed in two semi-infinite media; these two media are called *upper* and *lower* media [10]. In this case, the *upper* medium is free-space and the *lower* is a Perfect Electric Conductor (PEC). Here we define two layers, starting from the coordinate  $z = 0$ : the first of thickness  $d$ , with  $\epsilon_r$  of the current dielectric material, and the second of thickness  $\lambda/2$  with unitary  $\epsilon_r$ .

The solver gives as output the scattering parameters computed at the interfaces

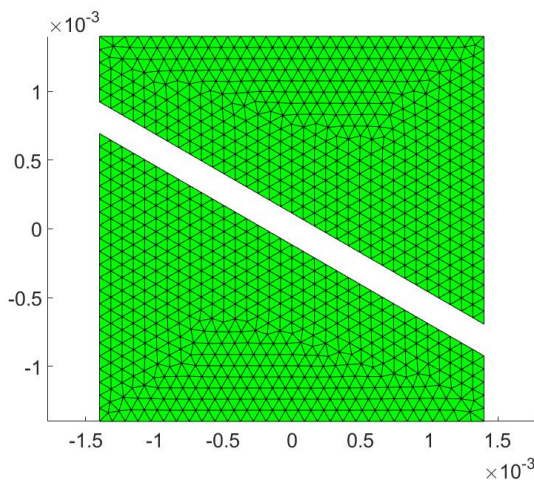


**Figure 2.2:** Mesh of the unit cell described in [1] produced for the in-house solver; all dimensions are in m

between the semi-infinite media and the structure; we label *port 1* the interface with the *upper* medium and *port 2* the interface with the *lower* medium. Since the

considered unit cell is PEC-backed, we are only interested in  $\mathbf{S}_{11}$ :

$$\mathbf{S}_{11} = \begin{bmatrix} S_{11}^{\text{TE,TE}} & S_{11}^{\text{TE,TM}} \\ S_{11}^{\text{TM,TE}} & S_{11}^{\text{TM,TM}} \end{bmatrix} \quad (2.6)$$

In particular, for normal incidence ( $\theta = 0^\circ$ ) the TM component of the electric field is directed along x while the TE term lies along y. Therefore, taking up the notation used before, we can easily compute the scattered electric field in terms of illuminations A and B:

$$E_x^{\text{As}} = S_{11}^{\text{TM,TM}} E_x^{\text{Ai}} \quad (2.7)$$

$$E_y^{\text{As}} = S_{11}^{\text{TE,TM}} E_x^{\text{Ai}} \quad (2.8)$$

$$E_x^{\text{Bs}} = S_{11}^{\text{TM,TE}} E_y^{\text{Bi}} \quad (2.9)$$

$$E_y^{\text{Bs}} = S_{11}^{\text{TE,TE}} E_y^{\text{Bi}} \quad (2.10)$$

where the superscripts i and s denote the incident and scattered field respectively, at the coordinate  $z = d + \lambda/2$ . Now we just have to de-embed the phase at the surface of the unit cell ( $z = d$ ), find the incident and scattered magnetic field using the impedance relation, compute the total fields and we can use eqs. (2.4)-(2.5).

In table 2.1 the tensor sheet impedance, i.e. the reciprocal of the sheet admittance matrix, is reported: the values obtained with CST and the in-house solver are compared to those listed in [1]. While there is close agreement between the results produced by CST and those of the aforementioned paper, a little discrepancy can be detected among the latter and the in-house solver outcome, in particular regarding  $\eta_{yy}^s$ . This, however, does not affect the applicability of the sheet extraction method within our in-house solver.

	CST	In-house solver	[1]
$\eta_{xx}^s$	-95.68j	-101.56j	-97.54j
$\eta_{xy}^s$	-47.01j	-50.48j	-47.73j
$\eta_{yx}^s$	-47.01j	-50.48j	-47.81j
$\eta_{yy}^s$	-173.12j	-185.65j	-176.40j

**Table 2.1:** Sheet impedance values corresponding to the simulated geometry; all values are in  $\Omega$

## 2.2 Sheet admittance from the scattering matrix

In [7] the relation between scattering parameters and sheet admittance is investigated.

Let's consider a metasurface consisting of a patterned metallic sheet placed at the interface between two regions with different wave impedances, namely  $\eta_1$  and  $\eta_2$ . Through Floquet ports normally incident plane waves are excited, hitting the sheet from both sides; this kind of simulations is easily performed with CST or the in-house solver described in the previous section. It can be shown that the sheet admittance is related to the scattering parameters (de-embedded to the patterned sheet) via the following expressions:

$$\begin{aligned} \mathbf{Y}_{\text{sheet}} &= \left( \frac{\mathbf{I} - \mathbf{S}_{11}}{\eta_1} - \frac{\mathbf{I} + \mathbf{S}_{11}}{\eta_2} \right) (\mathbf{I} + \mathbf{S}_{11})^{-1} \\ &= \left( \frac{\mathbf{I} - \mathbf{S}_{22}}{\eta_2} - \frac{\mathbf{I} + \mathbf{S}_{22}}{\eta_1} \right) (\mathbf{I} + \mathbf{S}_{22})^{-1} \end{aligned} \quad (2.11)$$

where  $\mathbf{I}$  is the identity matrix and

$$\mathbf{S}_{nm} = \begin{bmatrix} S_{nm}^{xx} & S_{nm}^{xy} \\ S_{nm}^{yx} & S_{nm}^{yy} \end{bmatrix} \quad (2.12)$$

is “a 2x2 matrix relating the field scattered into region  $n$  when a plane wave is normally incident from region  $m$ ” [7].

As an example, the geometry shown in fig.S3 (d) of the supplementary material of [7] is implemented and simulated with both the aforementioned solvers (fig. ??) and its sheet admittance is computed using eq. (2.11).

The obtained results are listed in table 2.2, where they are compared to the values reported in [7]. We can see that the sheet admittance values obtained with CST and the in-house solver are in close agreement and only slightly different from those of the paper.

	CST	In-house solver	[7]
$Y_{xx}^s \eta_0$	5.26j	5.26j	5.67j
$Y_{xy}^s \eta_0$	0j	0j	0j
$Y_{yx}^s \eta_0$	0j	0j	0j
$Y_{yy}^s \eta_0$	-2.34j	-2.23j	-2.63j

**Table 2.2:** Sheet admittance values corresponding to the simulated geometry

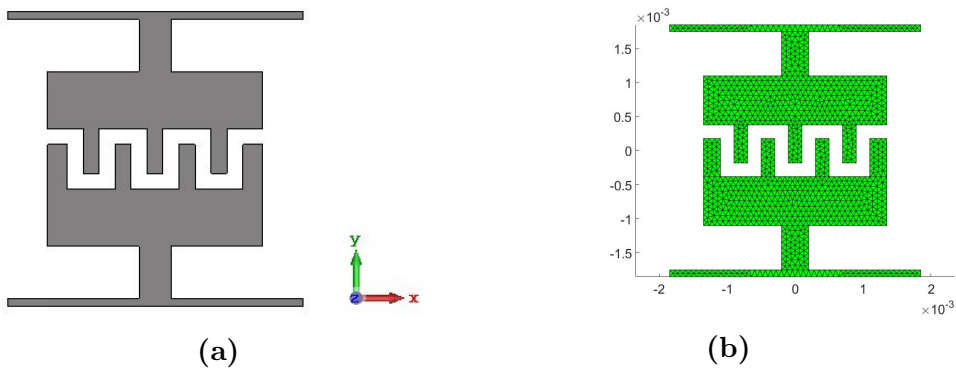


**Figure 2.3:** Unit cell in CST (a) and corresponding mesh for the in-house solver (b)

# Chapter 3

## Dispersion relation

In this chapter, different approaches are used to compute the wavevector of a TM surface wave sustained by a particular structure. In section 3.1 a Transverse Resonance Equation (TRE) is derived from a transmission-line equivalent model of the antenna. In section 3.2 the unknown wavevector is obtained from the enforcement of boundary conditions on the tangential electric and magnetic fields.

### 3.1 Transverse resonance technique

The transverse resonance technique relies on the derivation of an equivalent transmission-line model of the considered antenna. It stems from the interchangeability between tangential (to the structure) electric field and voltage and between tangential magnetic field and current. Here is an example.

#### 3.1.1 Example: mapping surface impedance to gap size

Let's consider the simple case of a SMRS consisting of an array of metallic strips separated by a varying gap, printed over a grounded dielectric substrate [2] of thickness  $d$ , lying in the  $xy$  plane. Let's also assume that this structure sustains a TM guided mode that propagates in the  $x$  direction. If we focus on a unit cell and consider its vertical stacking (ground, dielectric and metallic cladding) we can see that, for the electric and magnetic fields tangential to the surface  $E_x$  and  $H_y$ , it is equivalent to a vertical transmission line that extends along the  $z$  axis. This line starts at the bottom with a short circuit that represents the ground plane; at a distance  $d$  from it an admittance  $Y_{\text{SMRS}}$  corresponding to the modulated surface is inserted in parallel; then the line goes on to infinite as the free-space region that lies above the SMRS. This equivalent model is shown in fig. 3.1, where the semi-infinite transmission line that represents the free-space region above the antenna has been replaced by the TM wave admittance in air ( $Y_{00}^{\text{TM}}$ ), since that is what the SMRS

sees.

In particular, regarding the TM surface wave we can define the propagation

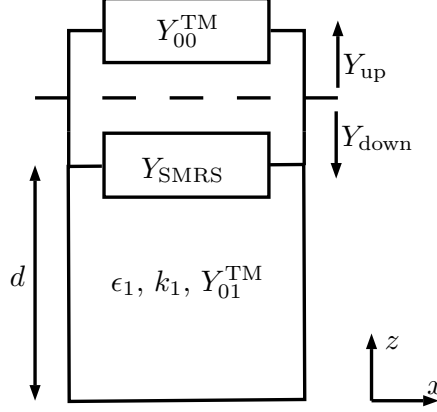


**Figure 3.1:** Equivalent transmission-line model of a SMRS printed on a grounded dielectric substrate, as the one described in [2]

wavenumber  $k_x$ , which is related to the transverse wavenumbers in free space ( $k_{z0}$ ) and in the dielectric ( $k_{z1}$ ) by the following expressions:

$$k_{z0} = \sqrt{k_0^2 - k_x^2} = -j\sqrt{k_x^2 - k_0^2} \quad (3.1)$$

$$k_{z1} = \sqrt{k_1^2 - k_x^2} \quad (3.2)$$

where  $k_0 = \omega\sqrt{\mu_0\epsilon_0}$  and  $k_1 = \omega\sqrt{\mu_1\epsilon_1}$ . By definition, a surface wave must be confined in the structure and attenuate away from it, therefore the transverse wavenumber in free space has to be purely imaginary and  $k_x$  must be in the range  $[k_0, k_1]$ . Now, we must define a reference section in the transmission line: in fig. 3.1 it is set right above the SMRS, at the interface between the antenna and the free space. The transverse resonance equation consists in setting equal to zero the sum of the admittance that you see looking up from the reference section ( $Y_{up}$ ) and the one that you see looking down ( $Y_{down}$ ):

$$Y_{up} + Y_{down} = 0 \quad (3.3)$$

where

$$Y_{up} = Y_{00}^{TM} \quad (3.4)$$

$$Y_{down} = Y_{SMRS} - jY_{01}^{TM} \cot(k_{z1}d) \quad (3.5)$$

and

$$Y_{00}^{\text{TM}} = \frac{\omega\epsilon_0}{k_{z0}} \quad (3.6)$$

$$Y_{01}^{\text{TM}} = \frac{\omega\epsilon_1}{k_{z1}} \quad (3.7)$$

Solving the TRE allows to find the propagation wavenumber  $k_x$  and therefore the surface impedance of the antenna, which is nothing more than the reciprocal of  $Y_{\text{down}}$ , for every value of  $Y_{\text{SMRS}}$ , i.e. every possible gap width between the strips that form the modulated reactance surface. As an example, the relation between gap spacing and surface reactance for the structure described in [2] at the frequency of 10 GHz is plotted in fig. 3.2. This graph is of great importance because it allows

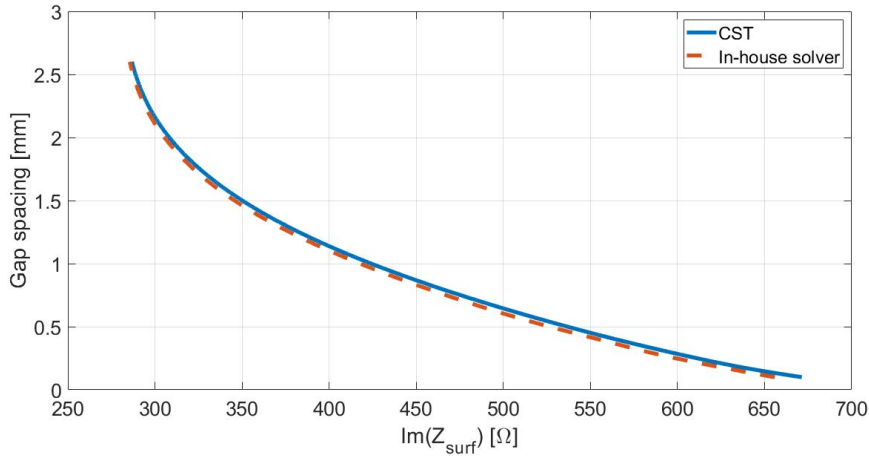


**Figure 3.2:** Gap spacing vs surface reactance for the antenna designed in [2] obtained with CST and in-house solver

to identify the physically achievable surface impedance range and to translate a sinusoidal modulation of the reactance into a varying geometrical parameter of the metasurface unit cell (gap width between the strips).

### 3.1.2 Application to our multi-layered antenna

The transverse resonance technique can be applied to our multi-layered antenna. Let's denote with  $Y_{\text{SMRS}}$  the sheet admittance of the upper layer and with  $Y_{\text{VAR}}$  the sheet admittance of the reconfigurable plane. Let  $d_0$  be the width of the air gap between ground and varactor layer and  $d_1$  the dielectric thickness. The equivalent transmission-line model of the overall structure for a TM mode is shown in fig. 3.3. As in the previously discussed example, the reference section is set right above the

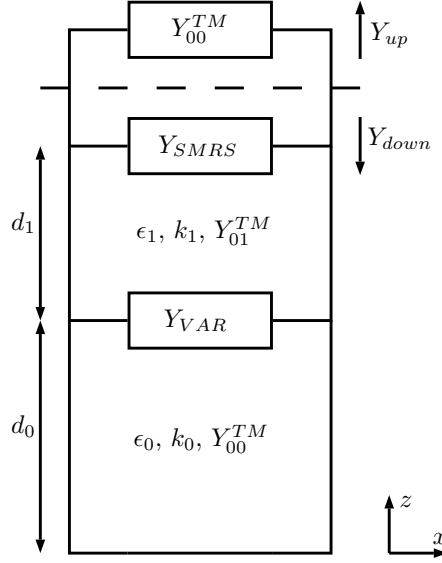


**Figure 3.3:** Transmission-line model of our multi-layered antenna

sinusoidally-modulated reactance surface. The admittance of the equivalent ground plane ( $Y_{\text{EGP}}$ ), composed by the fixed ground and the reconfigurable layer, is given by:

$$Y_{\text{EGP}} = Y_{\text{VAR}} - jY_{00}^{\text{TM}} \cot(k_{z0}d_0) \quad (3.8)$$

While  $Y_{\text{up}}$  has the same expression as before (eq. (3.4)),  $Y_{\text{down}}$  is the sum of  $Y_{\text{SMRS}}$  and the input admittance of a line of length  $d_1$  loaded with  $Y_{\text{EGP}}$ :

$$Y_{\text{down}} = Y_{01}^{\text{TM}} \frac{Y_{\text{EGP}} \cos(k_{z1}d_1) + jY_{01}^{\text{TM}} \sin(k_{z1}d_1)}{Y_{01}^{\text{TM}} \cos(k_{z1}d_1) + jY_{\text{EGP}} \sin(k_{z1}d_1)} \quad (3.9)$$

Eq. (3.3) can then be solved for the propagation wavenumber and the overall surface impedance of the antenna can be found.

## 3.2 Boundary conditions on tangential fields

The same results given by the transverse resonance technique can be derived, starting from the tangential electric and magnetic fields, by imposing boundary conditions.

Let's divide our structure in three regions, as depicted in fig. 3.4, and set the origin of the  $z$  axis at the interface between SMRS and free space. In region 1, the

tangential electric and magnetic fields  $\mathbf{E}_{t1}$  and  $\mathbf{H}_{t1}$  are:

$$\mathbf{E}_{t1} = (E_{01}^+ e^{-jk_{z0}(z+d_1)} + E_{01}^- e^{jk_{z0}(z+d_1)}) \hat{\mathbf{x}} \quad (3.10)$$

$$\mathbf{H}_{t1} = Y_{00}^{\text{TM}} (E_{01}^+ e^{-jk_{z0}(z+d_1)} - E_{01}^- e^{jk_{z0}(z+d_1)}) \hat{\mathbf{y}} \quad (3.11)$$

where the dependence on the x coordinate ( $e^{-jk_x x}$ ) has been omitted since it is common to all terms. The transverse wavenumbers  $k_{z0}$  and  $k_{z1}$  are expressed by eqs. (3.1)-(3.2).  $E_{01}^+$  and  $E_{01}^-$  are the amplitudes of the forward and backward waves in the z direction, defined at  $z = -d_1$ .

In a similar manner, the tangential fields in region 2 and 3 can be expressed as:

$$\mathbf{E}_{t2} = (E_{02}^+ e^{-jk_{z1}z} + E_{02}^- e^{jk_{z1}z}) \hat{\mathbf{x}} \quad (3.12)$$

$$\mathbf{H}_{t2} = Y_{01}^{\text{TM}} (E_{02}^+ e^{-jk_{z1}z} - E_{02}^- e^{jk_{z1}z}) \hat{\mathbf{y}} \quad (3.13)$$

$$\mathbf{E}_{t3} = E_{03}^+ e^{-jk_{z0}z} \hat{\mathbf{x}} \quad (3.14)$$

$$\mathbf{H}_{t3} = Y_{00}^{\text{TM}} E_{03}^+ e^{-jk_{z0}z} \hat{\mathbf{y}} \quad (3.15)$$

where the amplitudes  $E_{02}^+$ ,  $E_{02}^-$ ,  $E_{03}^+$  are all defined at  $z = 0$ . In region 3 there is only the wave propagating towards positive z because free space is infinitely extended and no reflection takes place.

At this point the boundary conditions at both the metasurfaces and the ground

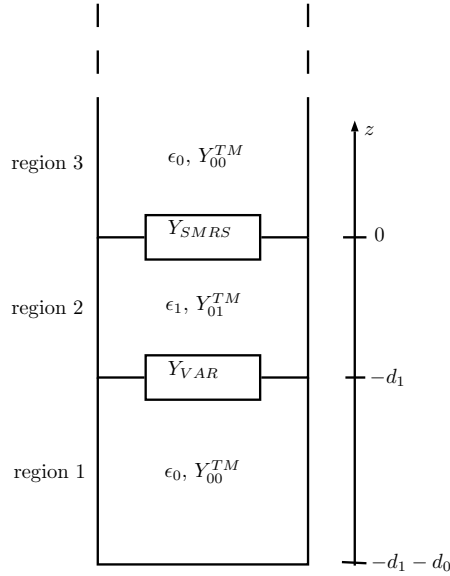


**Figure 3.4:** Vertical structure of our multi-layered antenna

plane must be enforced. Since we are dealing with purely electric admittance sheets, we have, at  $z = -d_1$  and  $z = 0$ , that the jump in the tangential magnetic field is

equal to the electric surface current density and that the tangential electric field must be continuous:

$$\hat{\mathbf{z}} \times (\mathbf{H}_{t3}(z = 0^+) - \mathbf{H}_{t2}(z = 0^-)) = Y_{\text{SMRS}} \frac{\mathbf{E}_{t3}(z = 0^+) + \mathbf{E}_{t2}(z = 0^-)}{2} \quad (3.16)$$

$$\hat{\mathbf{z}} \times (\mathbf{E}_{t2}(z = 0^-) - \mathbf{E}_{t3}(z = 0^+)) = 0 \quad (3.17)$$

$$\hat{\mathbf{z}} \times (\mathbf{H}_{t2}(z = -d_1^+) - \mathbf{H}_{t1}(z = -d_1^-)) = Y_{\text{VAR}} \frac{\mathbf{E}_{t2}(z = -d_1^+) + \mathbf{E}_{t1}(z = -d_1^-)}{2} \quad (3.18)$$

$$\hat{\mathbf{z}} \times (\mathbf{E}_{t1}(z = -d_1^-) - \mathbf{E}_{t2}(z = -d_1^+)) = 0 \quad (3.19)$$

Moreover, we must set the electric field to be null at  $z = -d_1 - d_0$ :

$$\mathbf{E}_{t1}(z = -d_1 - d_0) = 0 \quad (3.20)$$

Eqs. (3.16)-(3.20) form a five-equation system with five unknowns (the field amplitudes); in fact, they can be re-written as:

$$-Y_{00}^{\text{TM}} E_{03}^+ + Y_{01}^{\text{TM}} (E_{02}^+ - E_{02}^-) = Y_{\text{SMRS}} \frac{E_{03}^+ + E_{02}^+ + E_{02}^-}{2} \quad (3.21)$$

$$E_{02}^+ + E_{02}^- - E_{03}^+ = 0 \quad (3.22)$$

$$-Y_{01}^{\text{TM}} (E_{02}^+ e^{jk_{z1}d_1} - E_{02}^- e^{-jk_{z1}d_1}) + Y_{00}^{\text{TM}} (E_{01}^+ - E_{01}^-) = Y_{\text{VAR}} \frac{E_{02}^+ e^{jk_{z1}d_1} + E_{02}^- e^{-jk_{z1}d_1} + E_{01}^+ + E_{01}^-}{2} \quad (3.23)$$

$$E_{01}^+ + E_{01}^- - (E_{02}^+ e^{jk_{z1}d_1} + E_{02}^- e^{-jk_{z1}d_1}) = 0 \quad (3.24)$$

$$E_{01}^+ e^{jk_{z0}d_0} + E_{01}^- e^{-jk_{z0}d_0} = 0 \quad (3.25)$$

In matrix form:

$$\mathbf{M} \begin{bmatrix} E_{01}^+ \\ E_{01}^- \\ E_{02}^+ \\ E_{02}^- \\ E_{03}^+ \end{bmatrix} = \begin{bmatrix} 0 \\ 0 \\ 0 \\ 0 \\ 0 \end{bmatrix} \quad (3.26)$$

where:

$$\mathbf{M} = \begin{bmatrix} 0 & 0 & Y_{01}^{\text{TM}} - \frac{Y_{\text{SMRS}}}{2} & -(Y_{01}^{\text{TM}} + \frac{Y_{\text{SMRS}}}{2}) & -(Y_{00}^{\text{TM}} + \frac{Y_{\text{SMRS}}}{2}) \\ 0 & 0 & 1 & 1 & -1 \\ Y_{00}^{\text{TM}} - \frac{Y_{\text{VAR}}}{2} & -(Y_{00}^{\text{TM}} + \frac{Y_{\text{VAR}}}{2}) & -(Y_{01}^{\text{TM}} + \frac{Y_{\text{VAR}}}{2}) e^{jk_{z1}d_1} & (Y_{01}^{\text{TM}} - \frac{Y_{\text{VAR}}}{2}) e^{-jk_{z1}d_1} & 0 \\ 1 & 1 & -e^{jk_{z1}d_1} & -e^{-jk_{z1}d_1} & 0 \\ e^{jk_{z0}d_0} & e^{-jk_{z0}d_0} & 0 & 0 & 0 \end{bmatrix} \quad (3.27)$$

A nontrivial solution of (3.26) exists for the values of the propagation wavenumber  $k_x$  such that  $\det(\mathbf{M}) = 0$ . In fact, enforcing this condition allows to find the guided modes and also the field profile along the structure in the  $z$  direction.

# Chapter 4

## Design of a Sinusoidally-Modulated Reactance Surface

In this chapter, the procedure described in [2] is applied to design and simulate leaky-wave antennas based on a Sinusoidally-Modulated Reactance Surface (SMRS). The impedance modulation is achieved by varying a geometric feature of the metasurface unit cell, e.g. the gap width between metal strips [2] or the size of square patches [8]. The theory of SMRSs was first investigated by Oliner and Hessel [11]; here, only the principal results are reported in section 4.1. In section 4.2 two antennas based on different SMRSs are designed in order to radiate at  $\theta = 30^\circ$ . Finally, in section 4.3, the same procedure is applied to our multi-layered antenna in order to devise, once the upper layer physical implementation has been chosen, which values of sheet admittance of the reconfigurable plane are required to obtain the maximum possible steering of the leaky-wave beam.

### 4.1 Theory

Let's consider a surface whose reactance is modulated sinusoidally along the x axis. The expression of its reactance is:

$$X(x) = X_s \left[ 1 + M \cos \left( \frac{2\pi}{a} x \right) \right] \quad (4.1)$$

where  $X_s$  is the average surface reactance,  $M$  is the amplitude of modulation and  $a$  is the period. Let's suppose that the overall surface impedance is inductive in order to sustain a TM surface wave [2]. Since the structure is periodic, the total

field is given by the sum of infinite modes. Let's also define  $k_x$  as the propagation wavenumber of the fundamental mode in the x direction, which is related to the transverse wavenumber  $k_{zn}$  of the nth mode by:

$$k_{zn} = \sqrt{k_0^2 - \left(k_x + \frac{2n\pi}{a}\right)^2} \quad (4.2)$$

where  $k_0$  is the free-space wavenumber. It can be shown, starting from the transverse resonance condition, that the unknown modal currents  $I_n$  are linked by an infinite set of linear homogeneous equations [11]:

$$\begin{aligned} I_{n+1} + D_n I_n + I_{n-1} &= 0 \\ n &= 0, \pm 1, \pm 2 \dots \end{aligned} \quad (4.3)$$

where

$$D_n = \frac{2}{M} \left[ 1 - j \frac{k_{zn}}{X_s \omega \epsilon} \right] \quad (4.4)$$

System (4.3) has a nontrivial solution if its determinant is zero. Once the average reactance and the index of modulation have been chosen, solving this equation for the guided waves gives the Brillouin diagram, which allows to identify the radiating harmonics. An example of such diagram is shown in figure 4.1, for  $X_s = 1.2$  and  $M = 0.2$  as in [2].

In this graph we can see the radiation cone and the different spatial harmonics. At

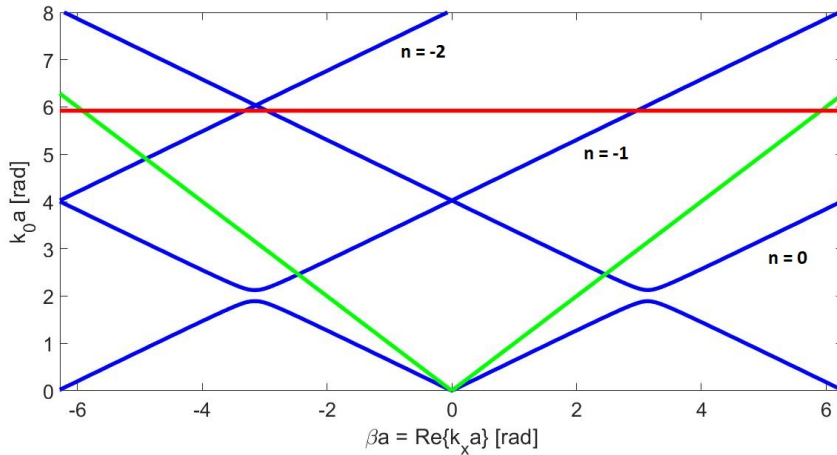


**Figure 4.1:** Brillouin diagram for  $X_s = 1.2$  and  $M = 0.2$ ; the blue curves correspond to the harmonics, the radiation cone is drawn in green, while the working point  $k_0 a$  is indicated by a red line

about  $k_x a = \pi \pm 2n\pi$  stop-bands appear, the width of which depends on the index of modulation  $M$ . In particular, we are interested in the  $n = -1$  harmonic: once we've established our working point (given by the operating frequency multiplied by the period of modulation), the main radiating beam of the leaky wave corresponds to the point belonging to this harmonic at the ordinate  $k_0 a$ . There can also be parasitic beams due to other harmonics; for example, in the case shown in fig. 4.1, an intersection between the red line and the  $n = -2$  harmonic inside the radiation cone is present, which indicates that also this mode radiates.

The first step in the procedure described in [2] to design a SMRS relies on the assumption that the modulation factor is zero, so that the following equation can be written:

$$\sin(\theta_{n=-1}) \approx \sqrt{1 + X_s'^2} - \frac{2\pi}{k_0 a} \quad (4.5)$$

where  $X_s'$  is the average surface reactance normalized by the free-space wave impedance. Once the working frequency, the desired radiation angle and one among  $X_s'$  or the period  $a$  have been fixed, eq. (4.5) can be used to determine the remaining value. To compute a more accurate value of the complex propagation wavenumber and, consequently, of the radiation angle, the determinantal equation of system (4.3) must be solved. Then, with the help of the Brillouin diagram, one must verify that the operating point  $k_0 a$  does not fall in the band-gap. Finally, the presence of other radiating harmonics must be checked.

## 4.2 Example: SMRS on a grounded substrate pointing at 30°

Following the procedure outlined in [2] the antenna designed in that paper is reproduced and simulated with CST (fig. 4.2). A sinusoidal modulation is physically realized by varying the gap width between parallel strips. To this purpose the graph in fig. 3.2 is used.

The radiated farfield at 10 GHz is shown in fig. 4.3. There is good agreement between this graph and the pattern reported in fig. 15 of [2].

Another possible implementation of a sinusoidally-modulated reactance surface is a texture of square patches with varying size [8]. This kind of surface is used to design an antenna radiating at 30° at the working frequency of 30 GHz.

The first step requires the computation of the sheet admittance of this surface. Using the technique described in **Chapter 2**, a unit cell made by a square patch printed on a grounded dielectric substrate (RO4003C) is implemented in both CST and in-house solver and two orthogonal illuminations are performed. From the obtained data, the sheet admittance is derived and plotted in fig. 4.4 as a function of the gap between two neighboring squares. Then, the transverse resonance equation must be solved for every value of the sheet admittance  $Y_{\text{SMRS}}$ , according to the

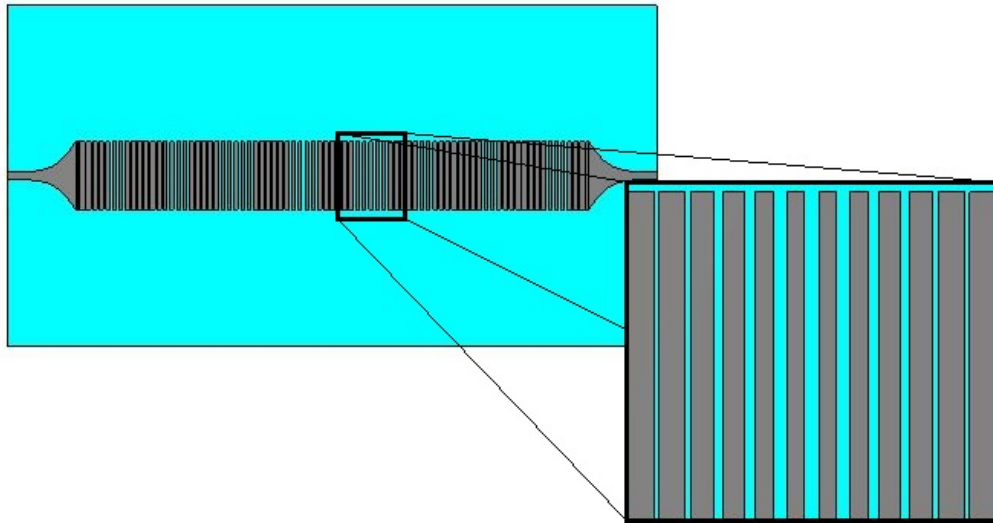


**Figure 4.2:** Simulated antenna with detail of the SMRS

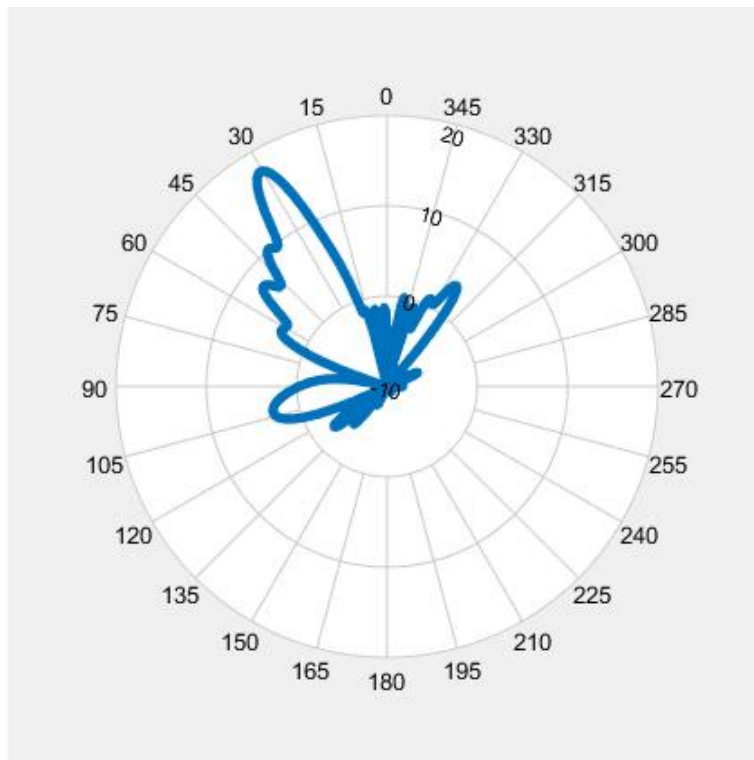


**Figure 4.3:** Radiation pattern (cut for  $\phi = 0^\circ$ ) of the antenna designed in [2]

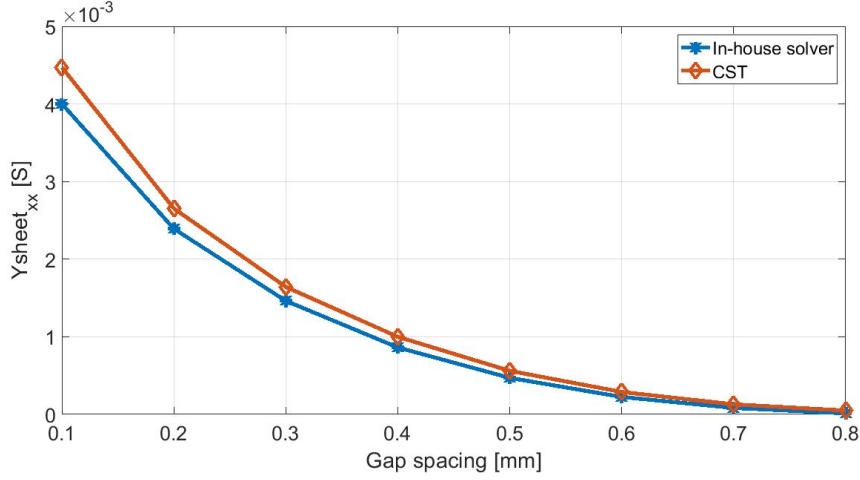


**Figure 4.4:** Sheet admittance of a texture of square patches as a function of the gap between them

transmission-line model represented in fig. 3.1; in this way we can obtain the mapping between gap spacing of the SMRS and surface impedance and we can translate the modulation of the latter into its physical implementation.

Once the dielectric material has been chosen, the surface impedance values derived from the solution of the TRE depend on the dielectric thickness  $d$ ; in particular, we want sufficiently high values of surface impedance so that there is only another harmonic radiating besides the  $n = -1$ . In fact, if we choose  $d = 0.508$  mm we get a possible range of surface impedance that goes from  $92.75\Omega$  to  $146.9\Omega$ ; then, if we select an average impedance  $X_s$  and a modulation factor  $M$  as to cover the whole range, we obtain a very large period ( $a = 18$  mm) and also the  $n = -3$  harmonic radiating, as can be seen from the Brillouin diagram represented in fig. 4.5. If we implement this kind of SMRS, the input power almost divides equally between the three radiating harmonics and the radiation pattern has a very low directivity and high side lobes (fig. 4.6).

The best choice is therefore to increase the dielectric thickness up to 1.016 mm; the mapping between gap spacing and surface impedance points to higher values of the latter (fig. 4.7), which allows to design a SMRS with a bigger average impedance. Only the  $n = -1$  and the  $n = -2$  harmonics are radiating, as you can see from the radiation pattern shown in fig. 4.8. A detail of the SMRS with square patches is shown in fig. 4.9. Overall there are no big differences between this implementation and the one with the array of strips, especially because the component of the sheet admittance of our interest ( $Y_{xx}^{sheet}$ ) is almost the same in both cases.

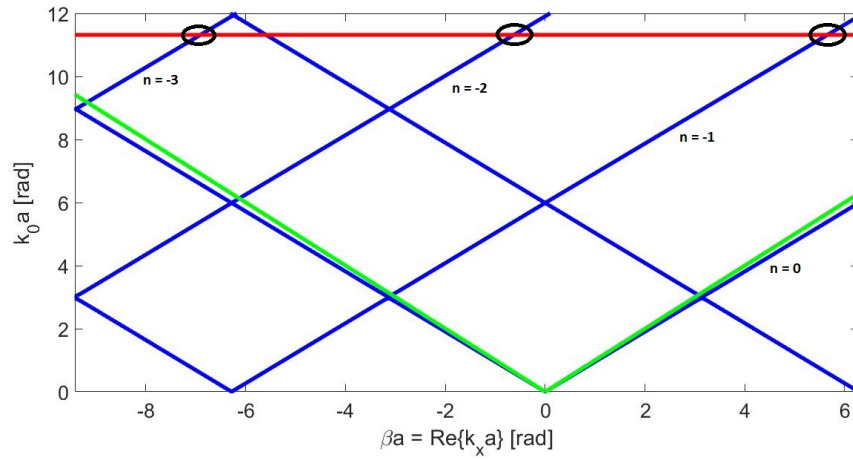


**Figure 4.5:** Brillouin diagram of a SMRS with  $X'_s = 0.3177$  and  $M = 0.22$

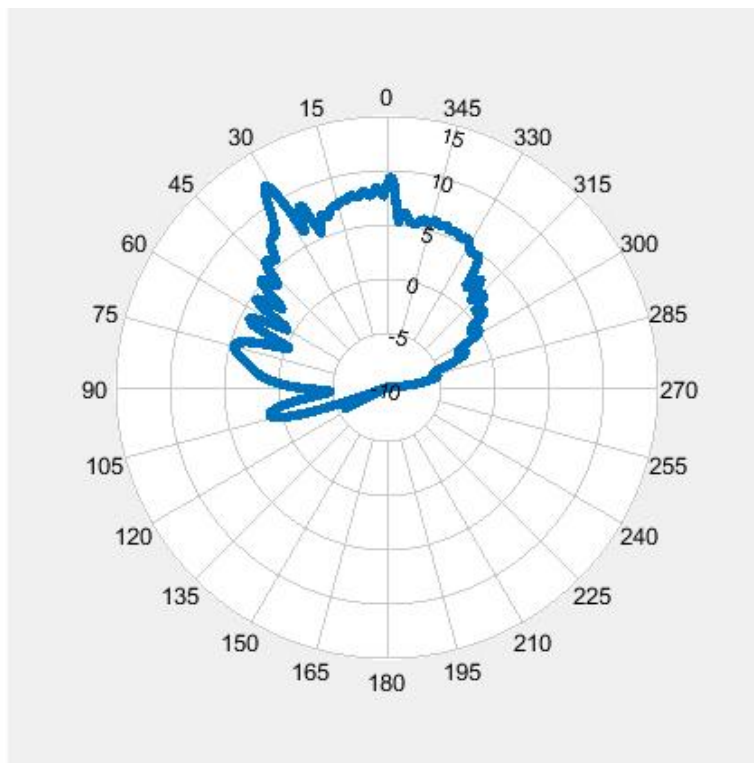


**Figure 4.6:** Radiation pattern for a printed leaky-wave antenna with  $X'_s = 0.3177$ ,  $M = 0.22$  and  $a = 18$  mm

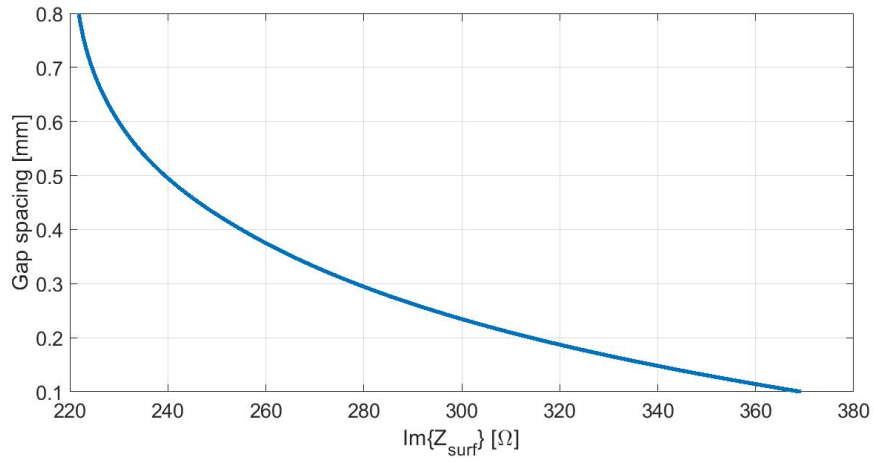


**Figure 4.7:** Mapping between gap spacing and surface impedance for a SMRS made by square patches with dielectric RO4003C and thickness equal to 1.016 mm

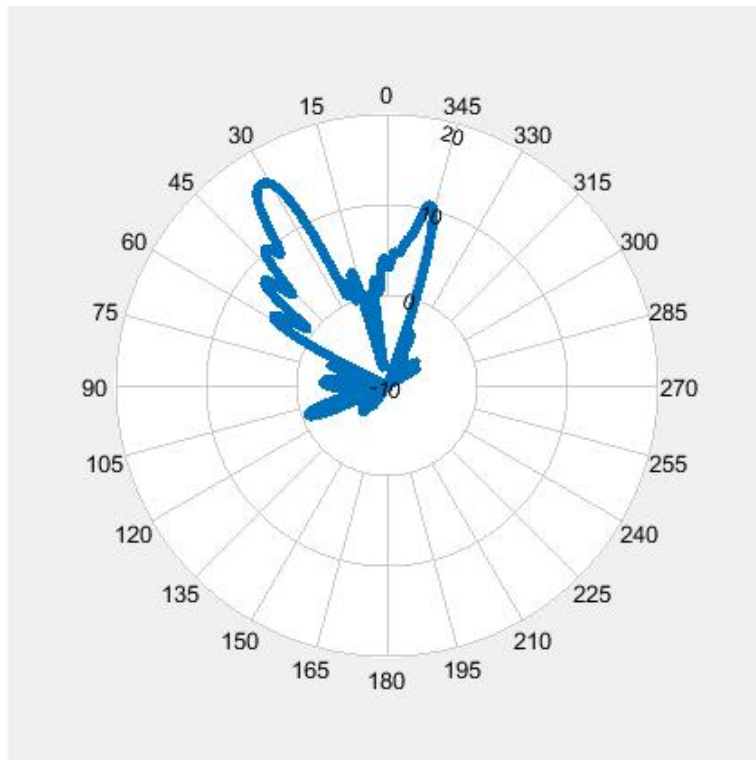


**Figure 4.8:** Radiation pattern (cut for  $\phi = 0^\circ$ ) of the antenna with square patches; the main beam points at  $32^\circ$

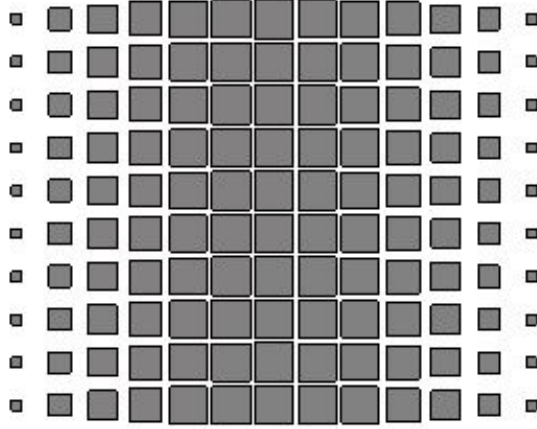


**Figure 4.9:** Detail of the SMRS with square patches

### 4.3 Application to our multi-layered antenna

The technique to design a SMRS outlined in the previous section can be applied to our multi-layered antenna, but first one needs to know the sheet admittances of the upper layer and the reconfigurable plane. In particular, it's important to gather which admittance values of the varactor layer are required to obtain a certain amount of steering of the main beam, regardless of their actual implementation. This analysis is carried out as follows:

1. The working frequency is set to be 30 GHz.
2. The physical implementation of the upper layer is chosen and its sheet admittance is computed.

We decide to use as SMRS the array of strips. To calculate the relation between sheet admittance and gap width we resort to the technique described in section 2.1: using both CST and the in-house solver we build a unit cell of dimension  $\lambda/10$  consisting of two strips separated by a gap printed on a grounded substrate made of the dielectric that is meant to be inserted in the complete multi-layered antenna. This is important because the sheet admittance of a metasurface depends on the media it is surrounded by [7]. In particular, we decide to use RO4003C ( $\epsilon_r = 3.55$ ). The dielectric thickness is chosen so that this extraction method is valid. Then from the input admittance the sheet admittance is derived using eq. (2.5); its behavior at varying gap width is shown in fig. 4.10.

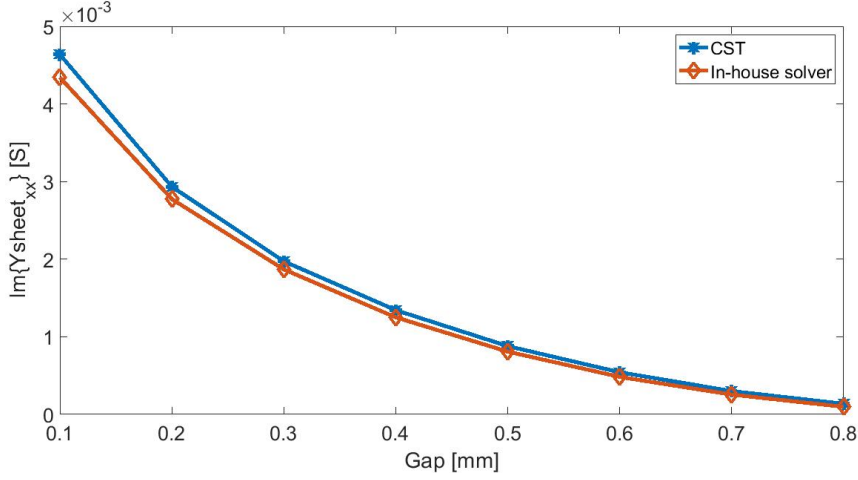


**Figure 4.10:** Sheet admittance vs gap spacing of the SMRS

- Once the sheet admittance of the upper layer ( $Y_{\text{SMRS}}$ ) is known, we must solve the transverse resonance equation of the overall structure for different values of the reconfigurable plane's sheet admittance ( $Y_{\text{VAR}}$ ) in order to identify the maximum possible steering of the radiating angle of our antenna.

To study the behavior of the solutions of the TRE as  $Y_{\text{VAR}}$  changes the other parameters must be fixed: referring to fig. 3.3, we set  $d_0 = \lambda/20 = 0.5$  mm (arbitrary value) and  $d_1 = 0.508$  mm (one of the standard thicknesses for this dielectric). The steerability of the antenna is evaluated as follows: for a given value of  $Y_{\text{VAR}}$ , the TRE is solved for each possible value of  $Y_{\text{SMRS}}$  in order to obtain a mapping between the physical gap width and the overall surface impedance, as shown in fig. 3.2 for a simpler structure; this surface impedance will fall into a particular range of values, whose limits depend on the considered  $Y_{\text{VAR}}$ . Now, we want the sheet admittance of the reconfigurable plane that gives the lower values of surface impedance to correspond to a radiating beam pointing at broadside ( $\theta = 0^\circ$ ); therefore, we compute the average reactance  $X_s$  as  $(Z_{\text{surf}}^{\text{max}} + Z_{\text{surf}}^{\text{min}})/2$  and, from eq. (4.5), setting  $\theta = 0^\circ$  we find the period  $a$ . The modulation factor  $M$  is calculated from  $Z_{\text{surf}}^{\text{max}} = X_s(1 + M)$ . Then the cosinusoid of eq. (4.1) is sampled in one period at points that are a tenth of a wavelength apart (the dimension of our unit cell) and each sample is mapped to the correspondent gap width. Once we've established the fixed gap width of every cell within one period for an antenna radiating at broadside for  $Y_{\text{VAR}}$  that gives the lower values of surface impedance, we can identify the main beam angle for the other values of  $Y_{\text{VAR}}$  by simply reversing the procedure: using the graph that shows the mapping between gap width and surface impedance, starting from the gaps we go back to the impedance;

then, by interpolating the obtained values with a cosine we extrapolate  $X_s$  and  $M$  and from those the radiating angle through eq. (4.1).

As for the sheet admittance of the varactor layer, two cases can be distinguished:

- (a)  $Y_{\text{VAR}} \geq 0$ : for positive values of  $Y_{\text{VAR}}$  there is only one solution of the TRE in the allowed range of  $k_x$ . This can be seen in fig. 4.11, where the blue curve represents  $-Y_{\text{up}}$  and the black curves depict  $Y_{\text{down}}$  for two different values of  $Y_{\text{VAR}}$ . The value of  $Y_{\text{SMRS}}$  is fixed and corresponds to a gap of 0.1 mm. The solution of the transverse resonance equation is given by the intersection between the blue curve and a black one. The

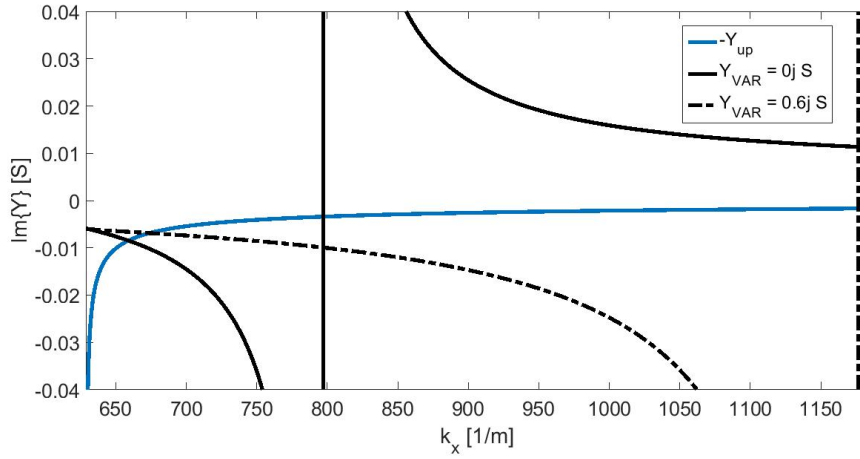


**Figure 4.11:** Solutions of the transverse resonance equation for gap of the SMRS equal to 0.1 mm and two different values of  $Y_{\text{VAR}}$

intersections are very close and there is no appreciable variation in the corresponding surface impedance (given by the reciprocal of  $Y_{\text{down}}$ ). In particular, if we design the antenna to radiate at broadside for  $Y_{\text{VAR}} = 0j$  S, for  $Y_{\text{VAR}} = 0.6j$  S the radiation angle is only  $2.75^\circ$ . If we increase further the sheet admittance of the reconfigurable layer this angle doesn't change.

- (b)  $Y_{\text{VAR}} < 0$ : for negative values of  $Y_{\text{VAR}}$  there are two solutions of the TRE (fig. 4.12), which correspond to two different TM modes. The solution closer to  $k_0$  belongs to the second TM mode, while the one closer to  $k_1$  identifies the first mode to go above cutoff. We are interested in the latter because it is the one that provides the most appreciable variation in terms of radiation angle. In fact, if we design the antenna to radiate at broadside for  $Y_{\text{VAR}} = -0.4j$  S, if  $Y_{\text{VAR}}$  reaches  $-0.013j$  S the radiation angle becomes  $36.93^\circ$ . It is worth noting that the greatest variation in the

surface impedance happens in a range close to  $-0.013j$  S: between  $Y_{\text{VAR}} = -0.4j$  S and  $Y_{\text{VAR}} = -0.04j$  S the steering is only of  $5.44^\circ$ . Moreover,  $-0.013j$  S is the maximum value of  $Y_{\text{VAR}}$  that is useful to our purpose: after that, there is no longer the solution of the TRE close to  $k_1$  for the smallest value of the SMRS gap, which means that the mapping between gap width and surface impedance will be discontinuous. Finally, going

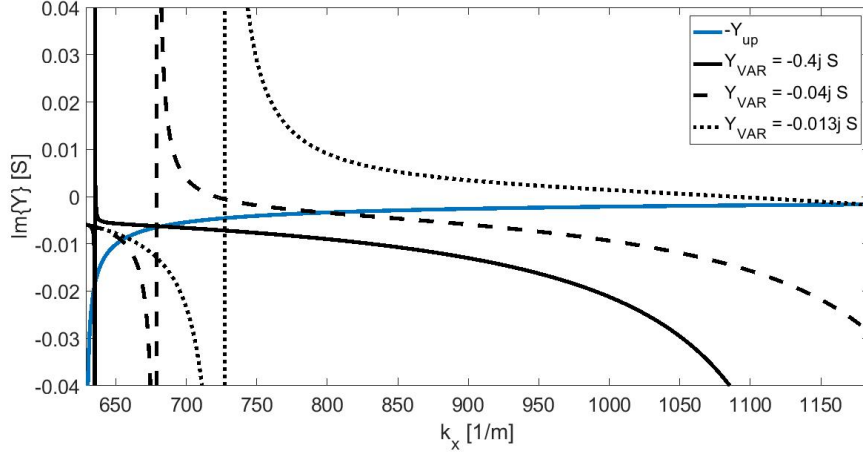


**Figure 4.12:** Solutions of the transverse resonance equation for gap of the SMRS equal to 0.1 mm and three different values of  $Y_{\text{VAR}}$

towards the limit value of  $Y_{\text{VAR}}$  the useful solution becomes unstable: the intersection between  $-Y_{\text{up}}$  and  $Y_{\text{down}}$  is grazing and more susceptible to errors. Therefore we might expect the steering of the antenna to be less accurate for large values of the radiation angle.

4. Once a suitable range of  $Y_{\text{VAR}}$  has been detected, the actual reconfigurable metasurface needs to be physically implemented. This will be done in **Chapter 5**.

To summarize, a range of negative values of  $Y_{\text{VAR}}$  has been identified which allows to steer the radiation angle of about  $30^\circ$ . This will be achieved by building a sinusoidally-modulated reactance surface, consisting of an array of metallic strips separated by a varying gap, on top of a reconfigurable metasurface, made so by the insertion of varactor diodes in the unit cell of such texture.

# Chapter 5

## Steerable leaky-wave antenna

In this chapter, a complete steerable leaky-wave antenna is simulated. First, in section 5.1 the unit cell of the reconfigurable layer is designed in order to achieve the suitable range of sheet admittance values which has been identified in **Chapter 4**. Then, in section 5.2, for discrete values of the varactor diodes' capacitance the radiation angle is computed solving the transverse resonance equation. The complete antenna is simulated and a clear steering of the main beam is observed; comparisons between expected and obtained results are made. Finally, in section 5.3 another version of the antenna is simulated which is equipped with a net of buses for the application of the control DC voltage to the diodes.

### 5.1 Implementation of the reconfigurable plane

In [12] a unit cell with two varactor diodes in antiseriess configuration is used as building block of a polarization rotator. The same schematic is resized and adjusted to our application and its sheet admittance is evaluated to see if the range of obtainable values is useful to our purpose.

A front view of such unit cell and its dimensions are reported in fig. 5.1. The dimensions are carefully designed in order to allow the placement of two diodes MAVR-011020-1141, whose capacitance is provided in their datasheet [13]. Overall the cell is a square of  $\lambda/5 \times \lambda/5$ , where  $\lambda = 10$  mm at the working frequency of 30 GHz. The size is bigger than  $\lambda/10$  in order to reduce the number of varactor diodes in the complete structure.

The sheet admittance of this metasurface is computed using the standard techniques described in **Chapter 2**. The diodes are modeled as RC series and the capacitance is swept starting from the minimum theoretical value of 0.025 pF. The admittance as a function of the capacitance is shown in fig. 5.2.

We can see that its values fall exactly in the range of our interest. In particular,

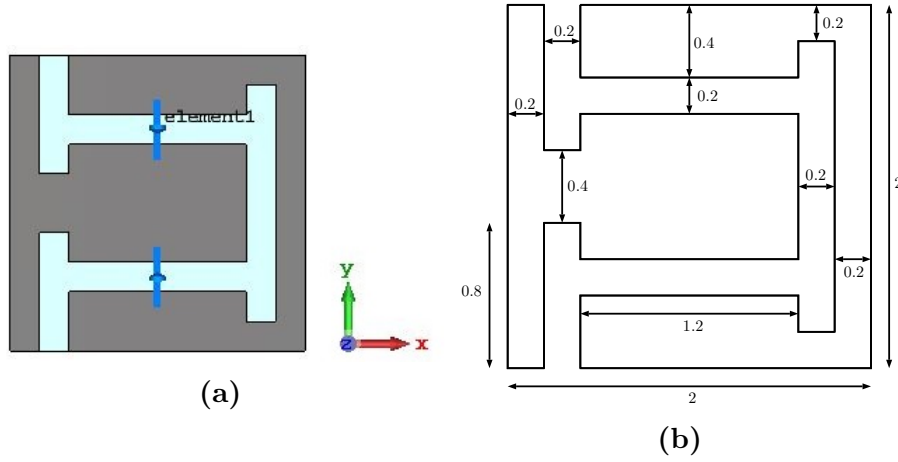


**Figure 5.1:** Unit cell of the reconfigurable layer: (a) front view and (b) dimensions (mm)

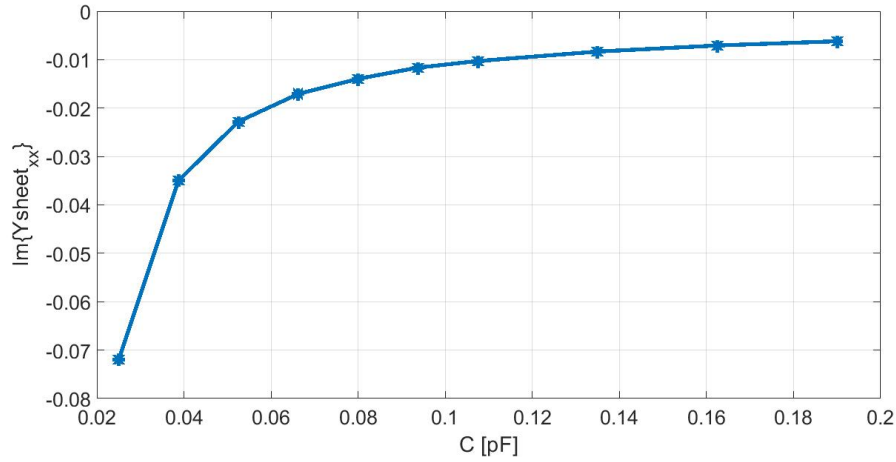


**Figure 5.2:** Sheet admittance of the reconfigurable metasurface with varying varactor capacitance

at  $C = 0.025$  pF  $Y_{\text{VAR}} = -0.072j$  S, while for a capacitance between 0.08 pF and 0.09 pF the limit value of about  $-0.013j$  is reached. Therefore, this unit cell proves itself to be an excellent candidate for the implementation of the reconfigurable layer of our antenna.

## 5.2 Simulation of the complete antenna

Solving the transverse resonance equation for every possible combination of gap width and varactor capacitance allows to study the modulation of the overall surface impedance and to visualize the steering of the radiation angle. The expected radiation angle of the main beam with varying varactor capacitance is shown in fig. 5.3.

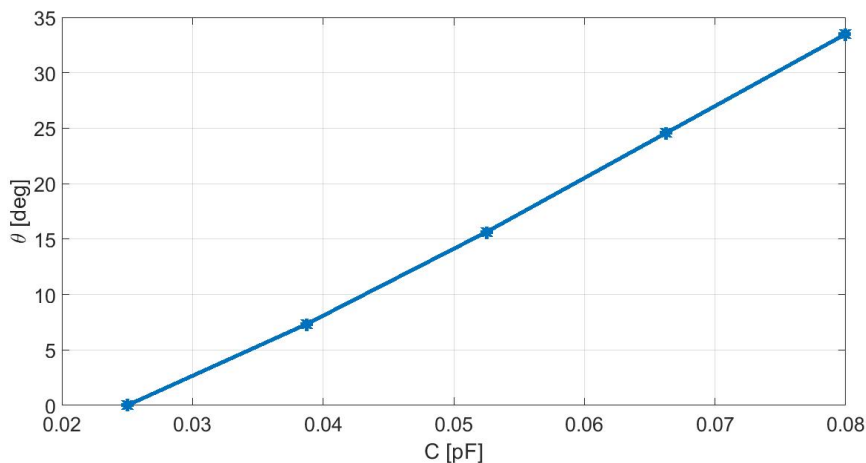


**Figure 5.3:** Expected steering of the main beam with varying varactor capacitance

A complete antenna is then built stacking up ground plane, reconfigurable layer and SMRS. The front view of the overall structure can be seen in fig. 5.4: the upper layer is made by the sinusoidally-modulated reactance surface, which is 8-period long; this ends with two feeders of length  $\lambda$  that are tapered down to  $50\Omega$  microstrips along the lines of what is done in [2]. The dielectric layer is larger than the SMRS, together with the ground plane. The reconfigurable metasurface extends below the SMRS and joins the ground plane below the feeder, as shown in fig. 5.5.

Finally, the complete antenna is simulated for different values of the varactor capacitance. Expected radiation angle, actual radiation angle, directivity and side lobe level are all listed in table 5.1. The resulting radiation patterns are shown in fig. 5.6. The difference between expected and simulated steering is highlighted by fig. 5.7.

Based on the data presented so far, some remarks can be made:

1. When the antenna is supposed to radiate at broadside (fig. 5.6a), as expected



**Figure 5.4:** Front view of the antenna: SMRS and dielectric layer are clearly visible

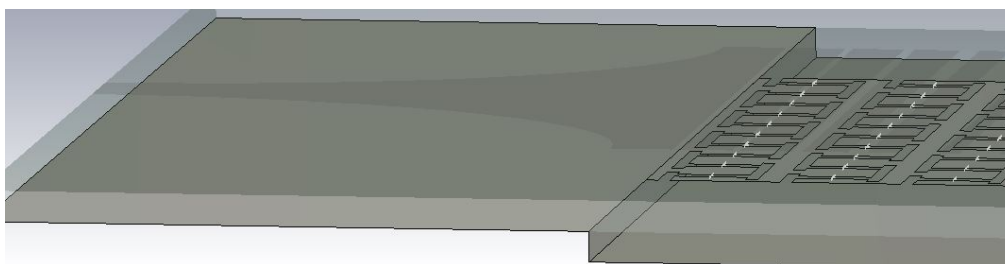


**Figure 5.5:** Detail of the blending between middle layer and ground plane right below the feeder

this does not happen because it is an intrinsic limit of the structure [2]: instead, we can see that the main beam is directed at  $\theta = 2^\circ$ , but the gain is very low and the side lobes really high.

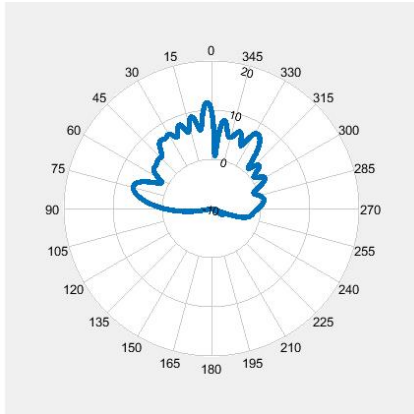
2. In general, for every considered value of the varactor diodes' capacitance, the radiation pattern is not very clean, since parasitic lobes of various intensity are present. This is due to two reasons: first, other than the  $n = -1$  harmonic, also the  $n = -2$  radiates and its beam is directed at a negative  $\theta$  (there is an intersection between the line  $k_0 a$  corresponding to the working point and the  $n = -2$  harmonic inside the radiation cone in the Brillouin diagram, as happens for the case depicted in fig. 4.1); second, the reflection coefficient  $S_{11}$  is high (around  $-10$  dB), therefore not all the input power ends up in the desired beam. The last problem could be solved by adjusting the structure of the feeder.
3. From fig. 5.7 it can be noticed that the simulated steering is a bit different from the expected one; in particular, while the two curves are quite close for radiation angles less than  $15^\circ$ , they start growing apart for bigger angles with an increasing divergence. This is due to the instability of the solutions of the transverse resonance equation for high values of the varactor capacitance, as

Capacitance	Expected $\theta$	Actual $\theta$	Directivity	Side lobe level
0.025 pF	0°	2°	11.6 dBi	-2.5 dB
0.03875 pF	7.3°	9°	14.5 dBi	-5.6 dB
0.0525 pF	15.6°	16°	15.9 dBi	-8.7 dB
0.06625 pF	24.6°	21°	15.6 dBi	-8.6 dB
0.08 pF	33.5°	25°	14.7 dBi	-4.6 dB

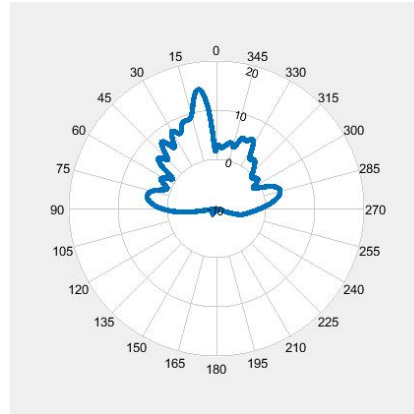
**Table 5.1:** Expected and simulated radiation angle, directivity and side lobe level for different values of the varactor capacitance

discussed in **Chapter 4**: a growing portion of the input power goes into the other solution, which corresponds to a negative radiation angle (about  $-4^\circ$ ).

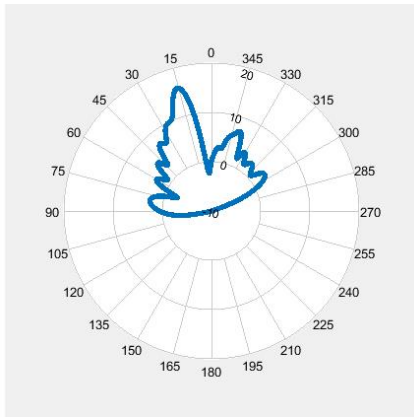
To sum it up, there is a clear steering of the main beam with varying varactor capacitance, however some problems emerge that require further study.



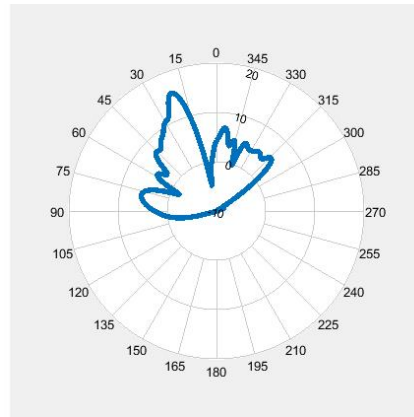
(a)  $\theta = 2^\circ$  for  $C = 0.025$  pF



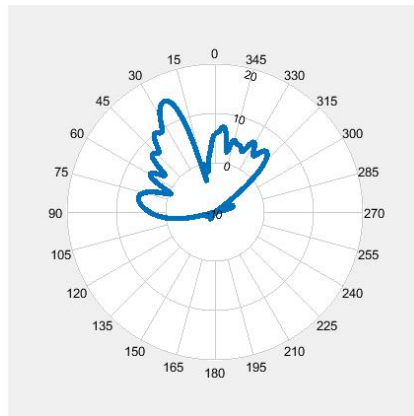
(b)  $\theta = 9^\circ$  for  $C = 0.03875$  pF



(c)  $\theta = 16^\circ$  for  $C = 0.0525$  pF



(d)  $\theta = 21^\circ$  for  $C = 0.06625$  pF



(e)  $\theta = 25^\circ$  for  $C = 0.08$  pF

**Figure 5.6:** Simulated farfield (cut for  $\phi = 0^\circ$ ) for different values of the varactor capacitance; the main beam steers from  $2^\circ$  (a) to  $25^\circ$  (e)

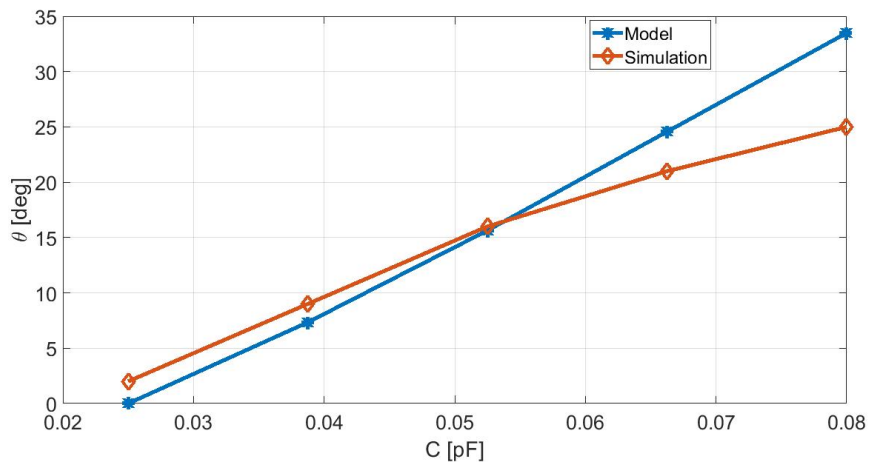


**Figure 5.7:** Expected vs simulated steering of the main beam with varying varactor capacitance

### 5.3 Simulation of the complete antenna with bus

A net of buses is introduced in the design of the antenna to allow the application of the DC control voltage to the varactor diodes (fig. 5.8). The lower bus connects strip alternatively to ground, while the upper one ties together the strips that will be connected to the control voltage, which is the same for all the devices. This newer version of our structure is then simulated to verify the impact of the buses on the overall performances. The results are listed in table 5.2, while the radiation pattern with varying varactor capacitance is shown in fig. 5.11.

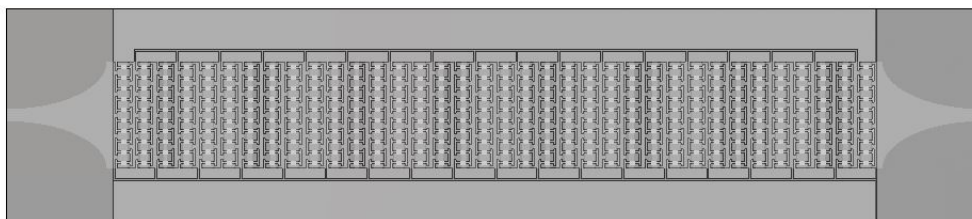


**Figure 5.8:** Front view of the reconfigurable layer (with ground plane in the background) with the addition of buses

Capacitance	Expected $\theta$	Actual $\theta$	Directivity	Side lobe level
0.025 pF	0°	1°	12.1 dBi	-2 dB
0.03875 pF	7.3°	8°	13.6 dBi	-5.7 dB
0.0525 pF	15.6°	15°	15.7 dBi	-8.3 dB
0.06625 pF	24.6°	19°	15.3 dBi	-4.4 dB
0.08 pF	33.5°	21°	13.9 dBi	-5.4 dB

**Table 5.2:** Expected and simulated radiation angle, directivity and side lobe level for different values of the varactor capacitance (antenna with buses)

Looking at the results in table 5.2, we can see that for this antenna the steering is reduced with respect to the implementation without bus. However, it is possible to try and increase the varactor diode's capacitance a bit more than before, for example up to 0.1 pF. In fact, for this capacitance value the useful solution of the transverse resonance equation is no longer available for the smallest gap width of the SMRS and therefore there is a discontinuity in the mapping between gap width and surface impedance (fig. 5.9); however, a single incorrect value in the cosinusoidal shape of the impedance does not alter the overall modulation, so it is possible to obtain a further steering in the main beam, even if it is lower than the

theoretical one, at the cost of a minor directivity and an increase in the side lobe level. The radiation pattern for  $C = 0.1$  pF is shown in fig. 5.10: the radiation angle is  $28^\circ$ , the directivity is 12.8 dBi and the side lobe level is  $-3$  dB.

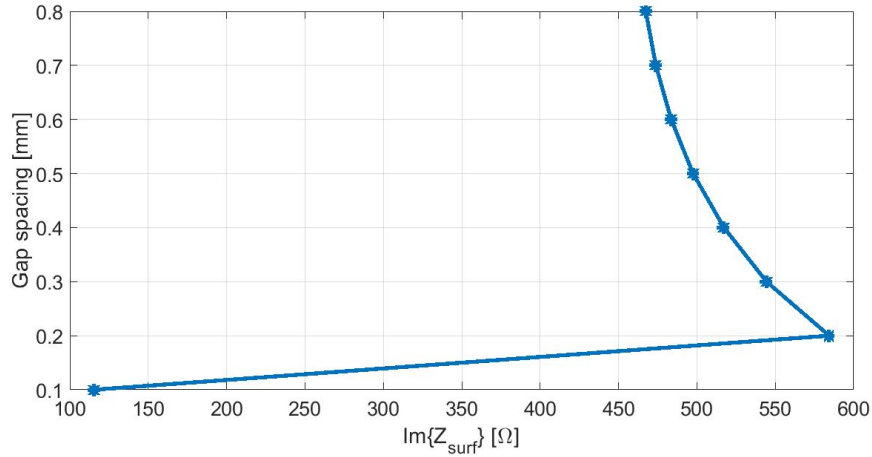


**Figure 5.9:** Example of the discontinuity in the mapping between gap width and surface impedance when the varactor capacitance (and therefore the sheet admittance  $Y_{\text{VAR}}$ ) exceeds a limit value

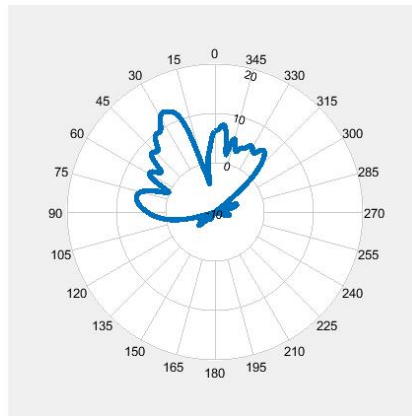
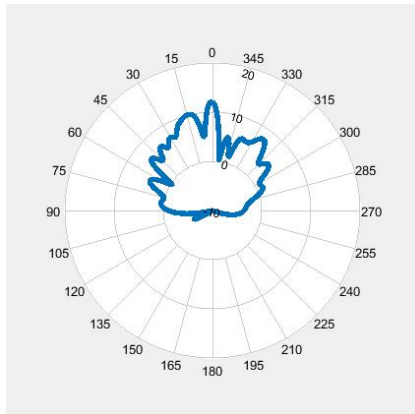


**Figure 5.10:** Radiation pattern for  $C = 0.1$  pF ( $\theta = 28^\circ$ )

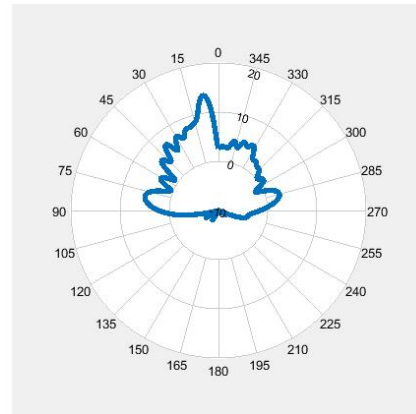
The comparison between expected and obtained steering for the antenna with buses is represented in fig. 5.12.

This antenna is now in the prototyping phase: fig. 5.13 shows the upper layer,

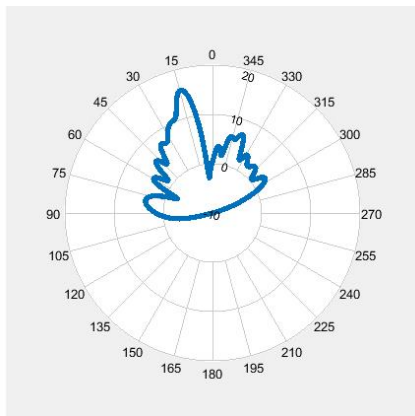
i.e. the SMRS, while fig. 5.14 represents the middle reconfigurable plane, where the diodes are placed.



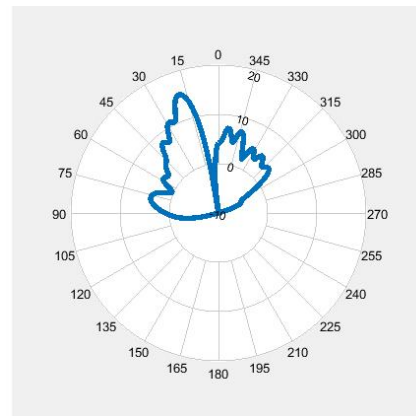
(a)  $\theta = 1^\circ$  for  $C = 0.025$  pF



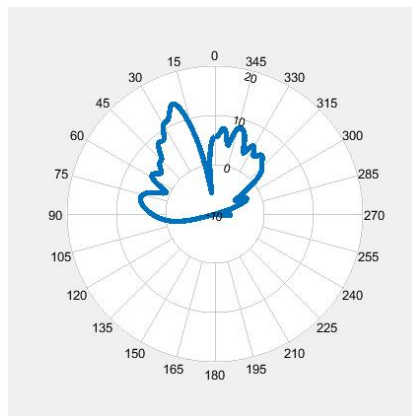
(b)  $\theta = 8^\circ$  for  $C = 0.03875$  pF



(c)  $\theta = 15^\circ$  for  $C = 0.0525$  pF



(d)  $\theta = 19^\circ$  for  $C = 0.06625$  pF



(e)  $\theta = 21^\circ$  for  $C = 0.08$  pF

**Figure 5.11:** Simulated farfield for different values of the varactor capacitance (antenna with buses); the main beam steers from  $1^\circ$  (a) to  $21^\circ$  (e)

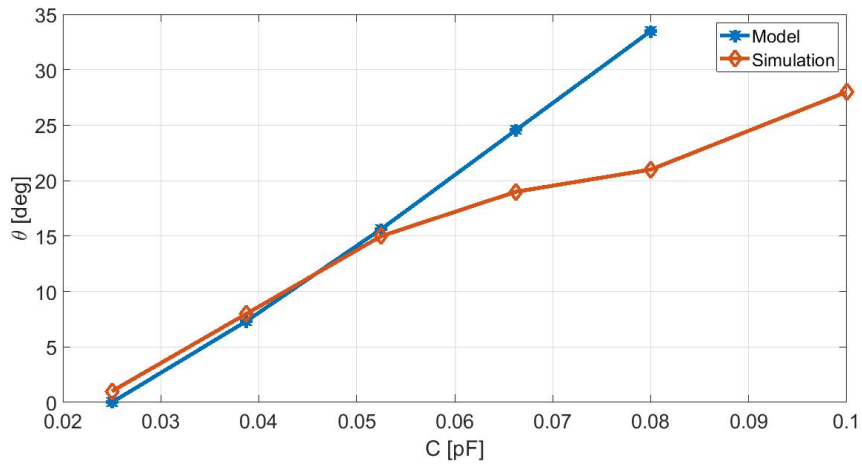


**Figure 5.12:** Expected vs simulated steering of the main beam with varying varactor capacitance for the antenna with buses

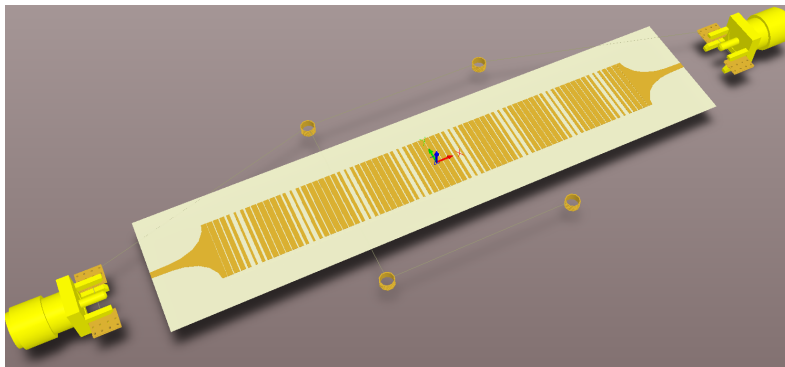


**Figure 5.13:** Upper layer of the steerable metasurface antenna

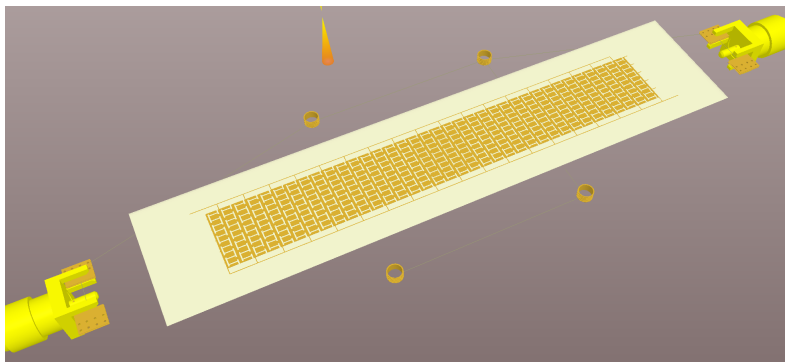


**Figure 5.14:** Reconfigurable plane of the steerable metasurface antenna

# Chapter 6

## Conclusions

In this thesis, a steerable metasurface antenna was designed and simulated. Several concepts were exploited, mainly leaky-wave radiation, surface impedance and transverse resonance technique. The main innovation was the introduction of a reconfigurable ground plane inside a multi-layered structure: varying the sheet admittance of such layer, thanks to the presence of varactor diodes, allowed to change the overall surface impedance of the antenna and therefore to steer the radiating beam. Although some discrepancies between the expected and the simulated results emerged, a clear steerability of the radiating beam was obtained.

Thanks to its flatness, small dimensions and high working frequency (Ka band), this particular antenna can prove itself to be a competitive solution for applications like satellite communications on-the-move. Bandwidth, power consumption and production cost have yet to be determined.

Despite the promising results, some improvements can be made in the perspective of future prototyping:

- improvement of the radiation pattern: this can be done using a uniaxial substrate and tailoring the leakage and phase constants along the antenna [14], or making a perfect conversion of a TM surface wave into a TM leaky wave through a surface reactance that varies from inductive to capacitive [15];
- better realization of the feeder, in order to reduce the reflection coefficient of the structure;
- further study on the choice of the dielectric and its thickness, to see if it's possible to obtain more stable solutions and a better matching between the expected and the simulated steering;
- use of a more accurate model of the varactor diode, that reflects its actual behavior;
- investigation of other types of sinusoidally-modulated reactance surfaces;

- focus on the vector nature of the sheet admittance instead of considering it as scalar.

# Bibliography

- [1] A. M. Patel and A. Grbic, “Modeling and Analysis of Printed-Circuit Tensor Impedance Surfaces,” *IEEE Transactions on Antennas and Propagation*, vol. 61, pp. 211–220, Jan. 2013.
- [2] A. M. Patel and A. Grbic, “A Printed Leaky-Wave Antenna Based on a Sinusoidally-Modulated Reactance Surface,” *IEEE Transactions on Antennas and Propagation*, vol. 59, pp. 2087–2096, June 2011.
- [3] O. Quevedo-Teruel *et al.*, “Roadmap on metasurfaces,” *Journal of Optics*, vol. 21, p. 073002, July 2019.
- [4] S. Maci, G. Minatti, M. Casaletti, and M. Bosiljevac, “Metasurfing: Addressing Waves on Impenetrable Metasurfaces,” *IEEE Antennas and Wireless Propagation Letters*, vol. 10, pp. 1499–1502, 2011.
- [5] D. Sievenpiper, Lijun Zhang, R. Broas, N. Alexopolous, and E. Yablonovitch, “High-impedance electromagnetic surfaces with a forbidden frequency band,” *IEEE Transactions on Microwave Theory and Techniques*, vol. 47, pp. 2059–2074, Nov. 1999.
- [6] A. A. Oliner and D. R. Jackson, “Leaky-wave antennas,” in *Antenna Engineering Handbook* (J. L. Volakis, ed.), McGraw-Hill, 2007.
- [7] C. Pfeiffer and A. Grbic, “Bianisotropic Metasurfaces for Optimal Polarization Control: Analysis and Synthesis,” *Physical Review Applied*, vol. 2, p. 044011, Oct. 2014.
- [8] Y. B. Li, L. L. Li, B. G. Cai, Q. Cheng, and T. J. Cui, “Holographic leaky-wave metasurfaces for dual-sensor imaging,” *Scientific Reports*, vol. 5, p. 18170, Nov. 2016.
- [9] “CST Studio Suite 2019.” [www.cst.com](http://www.cst.com). Dassault Systèmes Simulia.
- [10] A. Polemi, F. Vipiana, F. Caminita, S. Maci, F. Vernì, and G. Vecchi, “Square Unit Cell for Metasurfaces (MS) Design: Verification of Periodic Surface Spatial-Spectral Modeler (PSSM),” tech. rep., Politecnico di Torino, dec 2019.
- [11] A. Oliner and A. Hessel, “Guided waves on sinusoidally-modulated reactance surfaces,” *IRE Transactions on Antennas and Propagation*, vol. 7, pp. 201–208, Dec. 1959. Conference Name: IRE Transactions on Antennas and Propagation.
- [12] Z. Wu, Y. Ra’di, and A. Grbic, “Tunable Metasurfaces: A Polarization Rotator Design,” *Physical Review X*, vol. 9, p. 011036, Feb. 2019.

- [13] MACOM Technology Solutions. Solderable GaAs Constant Gamma Flip-Chip Varactor Diode, MAVR-011020-1411, <https://www.macom.com/products/product-detail/MAVR-011020-1411>.
- [14] B. B. Tierney and A. Grbic, “Arbitrary Beam Shaping Using 1-D Impedance Surfaces Supporting Leaky Waves,” *IEEE Transactions on Antennas and Propagation*, vol. 63, pp. 2439–2448, June 2015.
- [15] S. Tsvetkova, S. Tretyakov, and S. Maci, “Perfect conversion of a TM surface-wave into a TM leaky-wave by an isotropic periodic metasurface printed on a grounded dielectric slab,” *arXiv preprint arXiv:1907.03646*, 2019.
- [16] M. Faenzi, G. Minatti, D. González-Ovejero, F. Caminita, E. Martini, C. Della Giovampaola, and S. Maci, “Metasurface Antennas: New Models, Applications and Realizations,” *Scientific Reports*, vol. 9, p. 10178, Dec. 2019.
- [17] G. Minatti, F. Caminita, M. Casaletti, and S. Maci, “Spiral Leaky-Wave Antennas Based on Modulated Surface Impedance,” *IEEE Transactions on Antennas and Propagation*, vol. 59, pp. 4436–4444, Dec. 2011.